Extensive aqueous deposits at the base of the dichotomy boundary in Nilosyrtis Mensae, Mars

Joshua L. Bandfield[1] and Elena S. Amador[2]

[1]Space Science Institute
[2]Earth and Space Sciences, University of Washington, Seattle

Manuscript Correspondence:

Joshua Bandfield
Space Science Institute
4750 Walnut Street, Suite 205
Boulder, CO 80301, USA

jbandfield@spacescience.org

Manuscript Pages: 32
Figures: 13
Keywords: Mars, surface; Infrared observations; Spectroscopy; Mineralogy; Geological processes

Abstract

Thermal Emission Imaging System (THEMIS) and Compact Reconnaissance Imaging Spectrometer for Mars (CRISM) spectral datasets were used to identify high bulk SiO_2 and hydrated compositions throughout the Nilosyrtis Mensae region. Four isolated locations were identified across the region showing short wavelength silicate absorptions within the 8–12 μm spectral region, indicating surfaces dominated by high Si phases. Much more extensive exposures of hydrated compositions are present throughout the region, indicated by a spectral absorption near 1.9 μm in CRISM data. Although limited in spatial coverage, detailed spectral observations indicate that the hydrated materials contain Fe/Mg-smectites and hydrated silica along with minor exposures of Mg-carbonates and an unidentified hydrated phase. The high SiO_2 and hydrated materials are present in layered sediments near the base of topographic scarps at the hemispheric dichotomy boundary, typically near or within low albedo sand deposits. The source of the high SiO_2 and hydrated materials appears to be from groundwater discharge from Nili Fossae and Syrtis Major to the south, where there is evidence for extensive aqueous alteration of the subsurface. Although discontinuous, the exposures of high SiO_2 and hydrated materials span a wide area and are present in a similar geomorphological context to previously identified deposits in western Hellas Basin. These regional deposits may reflect aqueous conditions and alteration within the adjacent crust of the martian highlands.

Highlights

- THEMIS data show high SiO_2 compositions in isolated locations across Nilosyrtis Mensae
- CRISM data show extensive exposures of hydrated phases throughout the region
- Altered materials are in layered sediments at the base of the topographic boundary
- Groundwater discharge from Nili Fossae and Syrtis Major is a likely source
- The altered materials appear in a similar geologic context as in western Hellas Basin

1. Introduction

Spacecraft observations continue to reveal a wide variety of locations on Mars with evidence for past aqueous environments throughout its history. The increasingly detailed measurements and interpretations shed light on the specific conditions present at the time of formation. In particular, the identification of specific aqueous phases and their textural and morphological context can be used to determine specific environmental characteristics, such as the duration of exposure to water, pH, temperature, and chemical pathways. It is the combination of these factors that can be used to assess the potential for the development, sustenance, and preservation of life, in addition to assessing the geologic evolution of the planet.

Numerous exposures of aqueous phases have been identified across Mars (e.g., *Christensen et al.*, 2001; *Bandfield et al.*, 2003; *Gendrin et al.*, 2005; *Poulet et al.*, 2005; Milliken et al., 2008; *Ehlmann et al.*, 2008; *Bishop et al.*, 2008; *Osterloo et al.*, 2008; *Ehlmann et al.*, 2011; *Carter et al.*, 2013). In addition, *in situ* observations have been used to identify strong evidence for past aqueous conditions in regions where evidence from orbital measurements is faint or non-existent (e.g., *Ruff et al.*, 2011; *Morris et al.*, 2011). In many cases, these numerous exposures less than a few kilometers in scale, typically may be 10's or 100's of kilometers removed from their source (*Barnhart et al.*, 2011). In addition, with a few exceptions, the concentrations of the aqueous phases commonly appear to be low (<~10–15 areal %) based on near-infrared measurements and the lack of detection using orbital thermal infrared (TIR) spectral datasets (e.g., *Viviano and Moersch*, 2013; *Poulet et al.*, 2014). The isolated and potentially reworked nature of these materials can make it difficult to fully understand the formation environment.

More extensive exposures of aqueous phases have been identified, however. Many of these include laterally extensive layered sequences of sulfates and hematite similar to those investigated by the Mars Exploration Rover at Meridiani Planum (e.g., *Christensen et al.*, 2001; *Weitz et al.*, 2008; 2012). There are also several regions dominated by phyllosilicate and silica phases that include extended areas with high concentrations of materials (>~10–15%) that appear to have formed in-place. Mawrth Vallis is perhaps the most prominent example, covering ~10,000 km^2 with a range of phyllosilicate and silica compositions that indicate a variety of aqueous conditions (*Loizeau et al.*, 2007; *Bishop et al.*, 2008; *McKeown et al.*, 2009; *Farrand et al.*, 2009; *Noe Dobrea et al.*, 2010; *Michalski et al.*, 2013; *Viviano and Moersch*, 2013). Several extensive, but somewhat less prominent examples are also present on Mars. This includes Nili Fossae, where phases such as phyllosilicates and carbonates are exposed in bedrock units (e.g., *Mangold et al.*, 2007; *Mustard et al.*, 2009; *Ehlmann et al.*, 2009; *Viviano et al.*, 2013), and western Hellas Basin, where nearly pure hydrated silica is exposed sporadically along a 650 km stretch of the basin rim (*Bandfield*, 2008; *Bandfield et al.*, 2013).

Here, we use infrared spectroscopic datasets to identify another extensive region of hydrated and high bulk silica compositions near the martian hemispheric dichotomy boundary in the Nilosyrtis Mensae region. This is one of the largest regions of aqueous compositions found on the planet, including numerous isolated exposures, and a region of nearly continuous hydrated compositions stretching for ~300 km along the dichotomy boundary. The mineralogy and morphological context bears similarities to previously described regions in western Hellas Basin and nearby in Nili Fossae (*Ehlmann et al.*, 2009; *Mustard et al.*, 2009). Some of the surface compositions in this region have been described in previous work and Nilosyrtis Mensae has been proposed as a landing site because of its mineralogical diversity (e.g., *Summary Report for the First MSL Landing Site Workshop* available at http://marsoweb.nas.nasa.gov/landingsites/msl/workshops/1st_workshop/docs/MSL_workshop_report.pdf). Despite this, the extensive nature and high concentrations of the exposures have only been briefly described to date (*Poulet et al.*, 2008; *Ehlmann et al.*, 2009).

2. Data and methods

2.1 THEMIS data

The Thermal Emission Imaging System (THEMIS) consists of a 320 by 240 element uncooled microbolometer array with 9 spectral channels centered at wavelengths from ~7 to 15 μm (Table 1) and a spatial sampling of 100 m/pixel. Multispectral images are collected in a pushbroom configuration with rows of detectors under each spectral filter co-added to increase the signal to noise ratio. Detailed descriptions of calibration methods and radiometric uncertainties are presented in *Christensen et al.* (2004), *Bandfield et al.* (2004a), and *Edwards et al.* (2011).

Our analyses used THEMIS data acquired at afternoon local times of ~1400–1800 H and near-nadir observation geometries. We only examined images with full spectral coverage and an average temperature >220K for spectral diversity and features of interest. Using these criteria, all regions of interest investigated here (described in Section 3.1.1) have full surface coverage and many surfaces have repeat coverage. We did not place restrictions on atmospheric water ice or dust loading for THEMIS image selection, but the images used for detailed analyses all have 9 μm dust opacities of <0.16 and 11 μm water ice opacities of <0.05.

We employed several methods that use multispectral THEMIS images to identify surfaces with a high bulk SiO_2 content. First, we used decorrelation stretch (DCS) images (*Gillespie et al.*, 1986), to rapidly identify spectrally unique surfaces using calibrated radiance data without the need for the extensive processing typically required for producing atmospherically corrected surface emissivity (e.g., *Hamilton and Christensen*, 2005; *Bandfield et al.*, 2004b; *Rogers et al.*, 2005; *Bandfield*, 2008; *Osterloo et al.*, 2008). The high bulk SiO_2 surfaces of interest to this study have relatively low emissivity values at wavelengths corresponding to THEMIS band 4 within the ~8–12 μm Si–O asymmetric stretch Reststrahlen band. By contrast, basaltic and dusty surfaces have low emissivity values in THEMIS bands 6–8 and 2 respectively. These differences in emissivity result in color differences between the three compositional types. We constructed color DCS images from THEMIS band 6–4–2, 8–7–5, and 9–6–4 radiance images to cover a wide spectral range and distinguish between the different surface types. Using these three band combination images, the high SiO_2 surface types appear as magenta, yellow, and yellow respectively.

Although the DCS images are useful for the rapid identification of spectrally unique surfaces, we applied other techniques to the THEMIS data in order to confirm their presence and derive quantitative parameters from the data. We first correct the THEMIS data for atmospheric effects using the methods of *Bandfield et al.* (2004b) in order to derive surface emissivity. We used the surface emissivity data in two ways; 1) direct analysis of THEMIS surface emissivity spectra and comparison with previously described Mars thermal infrared (TIR) spectral types, and 2) production of weighted absorption center (WAC) images.

Surfaces with relatively low emissivity near 8 μm (THEMIS band 3) typically result in spectra with band 1–2 emissivity values greater than one. This is a result of our assumption that the maximum surface emissivity occurs in THEMIS bands 3–9, neglecting bands 1–2 for surface kinetic temperature determination. Although it is clear that this is can be an incorrect assumption, the measured radiance is typically low in these bands. Consequently, they have the potential to map significant inaccuracies in the other bands if they are used for surface temperature determination. A relatively low emissivity in band 3 compared to bands 1–2 can be inferred where the emissivity of THEMIS bands 1–2 is greater than one throughout this work, consistent with the presence of shorter wavelength absorptions.

The WAC images use the overall shape and position of the 8–12 μm Reststrahlen Si–O absorption present in THEMIS data to estimate the relative SiO_2 content of the surface materials. This technique takes advantage of the inverse correlation between the wavelength position of the Si–O absorption and SiO_2 content (*Vincent and Thomson*, 1972). Each WAC value is calculated from the integrated area of the spectral absorption present in the surface emissivity of THEMIS bands 3–9. The WAC wavelength is where half of the absorption area is present at longer wavelengths and half is present at shorter wavelengths. This technique is similar to that developed by *Vincent and Thomson* (1972) and has been applied previously to THEMIS surface emissivity data by *Smith et al.* (2013) and *Amador and Bandfield* (2015). This is also similar to the spline fit minimum emissivity technique of *Pan et al.* (2015) and *Rogers and Nekvasil* (2015). One advantage of this technique is that it reduces the THEMIS data to a single quantitative parameter that can be directly compared with spectral measurements of other surfaces and materials. The work of Vincent and Thomson (1972) focused on igneous compositions and it is not clear how accurate quantitative retrievals of SiO_2 would be using the WAC parameter. However, given the limited spectral resolution of the THEMIS data, we use the WAC parameter to succinctly summarize silicate diversity in a region.

For the THEMIS data that we used in this work, spectrally uniform regions show standard deviations in WAC values of <0.04 µm. Systematic errors are most likely caused by incorrect removal of the effects of atmospheric dust. For example, an error of -0.01 in dust opacity results in a change of -0.075 µm for WAC values of 10.5 µm and -0.025 for WAC values of 9.7 µm. Errors in atmospheric correction have little influence on the retrieved WAC values because the atmospheric dust has a WAC value similar to the high SiO_2 surfaces that we focus on here.

2.2 CRISM data

CRISM is a scanning imaging spectrometer covering wavelengths of 0.362–3.92 µm at 0.00655 µm sampling. We used full- and half-resolution targeted (FRT, HRL, HRS) near-infrared (~1.0–3.9 µm) I/F TRR3 data products, which include full spectral coverage at ~18 or 36 m/pixel sampling. We also used multispectral survey products (MSP), which sample 55 wavelengths between ~1.0 and 3.5 µm at 200 m/pixel sampling. A more complete description of the CRISM instrument and science investigation can be found in *Murchie et al.* (2007).

We corrected all data for atmospheric gas absorptions using the "volcano scan" method similar to that described by *McGuire et al.* (2009). Additional data processing is performed using algorithms that we adapted from the CRISM Analysis Tool (CAT) version 7.2.1, available at the Planetary Data System (PDS). These algorithms include two additional optimizations to correct for atmospheric gas spectral features: 1) The volcano scan observation used for the correction is selected to minimize artifacts in the corrected data. This algorithm searches a catalog of all volcano scan observations, rather than simply using observations acquired during a similar time period or instrument temperature as the data to be corrected. 2) The volcano scan correction is further improved by scaling and subtracting an artifact spectrum (located in the corresponding CRISM ADR file along with the volcano scan derived atmospheric transmission spectrum) from the data. The artifact spectral shape is necessary to account for inaccuracies in the spectral shape derived from the volcano scan observations.

We produced spectral index images from the CRISM data in a manner similar to that described by *Pelkey et al.* (2007) and *Viviano-Beck et al.* (2014). For the multispectral survey images, we rely primarily on the BD1900 index, which is used to map the strength of an absorption near 1.9 μm wavelengths due to O–H and H_2O vibrational overtones. This absorption is not particularly diagnostic of specific hydrated compositions, but it is relatively prominent and easy to detect, and can be used to identify the presence of a wide variety of hydrated phases that are of interest for this work.

We use additional spectral indices for the identification and mapping of specific phases in the full- and half-resolution CRISM data, where they are available for surfaces of interest. In particular, the D2300, BD2290, and MIN2250 (*Viviano-Beck et al.*, 2014) indices are used to identify and map phyllosilicate and hydrated silica phases. For the work presented here, we use the average (as opposed to median filtering) of the spectral channels listed by *Viviano-Beck et al.* (2014). Although these indices can also be applied to the CRISM multispectral survey data, we find them to be less reliable due to the higher noise present in the data and relatively subtle nature of the spectral features.

Several image processing steps are applied to the MSP images that enable visual identification of surfaces with enhanced 1.9 μm spectral absorptions. We produced index images using a standard deviation stretch to show the relative variation within a scene. Each image was stretched uniquely using a linear transformation to draw attention to local variations in the index values, though this prevents quantitative comparison of index values between images. We found this necessary to account for variable atmospheric conditions throughout the martian year that make it impossible to directly compare images without the application of more rigorous atmospheric compensation methods. CRISM data are acquired under a variety of viewing geometries, further complicating comparison between images that are not corrected for atmospheric aerosols. In addition, we subtracted the column average from the index images to remove persistent lateral gradients in index image values. Finally, in the case of the MSP data, we apply a 3 by 3 pixel median filter to the resulting image to reduce the effect of noise spikes that are common. This filter effectively de-speckles the data, though it also reduces the effective spatial resolution. We use the index images for qualitative purposes only because of these processing steps and the multiple interpretive links between the index value and the actual surface abundance of the phase of interest.

Where the indices display evidence for a particular phase of interest, we inspect the individual I/F spectra. It is necessary to manually inspect plotted spectra to ensure that the index value is not influenced by systematic noise, atmospheric effects, or the presence of other surface compositions that would lead to false identifications. To cancel residual noise and most atmospheric effects, we produced spectral ratios using a nearby surface (with the same detector array columns) as the denominator. Although we make an effort to avoid surfaces with clear and distinct spectral absorptions, no surface on Mars is spectrally neutral and spectral ratios can be a complex mixture of positive and negative absorption features. However, in practice, this is an effective method for the identification of narrow and prominent absorptions, such as those present in many hydrated phases and carbonates at near-infrared wavelengths (e.g., *Poulet et al.*, 2005; *Murchie et al.*, 2007; *Milliken et al.*, 2008; *Ehlmann et al.*, 2008; *Bishop et al.*, 2008; *Smith and Bandfield*, 2012).

Visual identification of spectral absorptions for the presence of any particular phase can be subjective. For this work, a confident detection relies on instances where the spectral shape is clearly defined to ensure only potential errors of omission in our results. For example, the presence of clearly identifiable 1.9 and ~2.25 μm absorption features with a similar width and asymmetry to that of laboratory spectra (e.g, *Rice et al.*, 2013; *Smith et al.*, 2013) would lead to our interpretation of the presence of opaline silica. Finally, the definition of spatial boundaries for surface typess are subject to similar subjective criteria, but in most cases, surface compositional boundaries are well-defined over hundred meter to kilometer scales.

2.3 HiRISE and CTX images

We also use visible wavelength imaging data from the High Resolution Imaging Science Experiment (HiRISE; *McEwen et al.*, 2007) and the Context Camera (CTX; *Malin et al.*, 2007) on-board the Mars Reconnaissance Orbiter (MRO) to characterize surface textures and morphology. We use HiRISE images (sampled at ~0.25-0.5 m/pixel) to identify fine-scale surface textures and features such as individual sediment layers and boulders. HiRISE data coverage is extremely limited in the regions we investigated, but is usually acquired along with full- and half-resolution CRISM images. We more typically relied on CTX images (sampled at ~5.5 m/pixel) for surface morphological and textural information because of their broad and nearly complete spatial coverage.

3. Results

3.1 THEMIS data

3.1.1 DCS and WAC images

Our survey used all THEMIS images near the highlands-lowlands boundary between 335°E and

85°E. This included elevation ranges of -4000 to 0 m using the image selection constraints described in Section 2.1. Fourspectral types were identified. The type of interest for this study appears magenta, yellow, and yellow in DCS images, using THEMIS bands 6–4–2, 8–7–5, and 9–6–4, respectively. This color combination indicates the presence of more prominent spectral absorptions in bands 4 and 5 relative to the other bands. Four locations in our study area (TIR regions a–d from west to east) show this sequence of colors in the THEMIS images although in some cases this spectral type can appear orange in THEMIS bands 9–6–4 DCS images (Figures 1 and 2; Table 2). In all cases, surfaces with these spectral characteristics are located immediately adjacent to surfaces that appear cyan, magenta, and magenta in the three THEMIS DCS image band combinations. This second spectral type is much more extensive and coincides with low albedo surfaces throughout the region. These spectral properties are consistent with relatively strong absorptions present in THEMIS bands 6 and 7. The third spectral type appears primarily as various hues of green in all three DCS band combinations. This spectral type has low spectral contrast in all THEMIS bands except at the shortest wavelengths (THEMIS bands 1–2)

A fourth spectral type is present in region d, near 79.9°E, 24.5°N, and appears green, purple, and blue in the three THEMIS DCS image band combinations. This occurs in a small exposure near the Nili region, where extensive olivine-rich basalts are present (*Hoefen et al.*, 2003, *Hamilton et al.*, 2003; *Hamilton and Christensen*, 2005; *Mustard et al.*, 2009). We will not consider this type further because it only occurs in one isolated instance within our study area and appears disconnected from the surface type that is the focus of this work.

We produced weighted absorption center images, covering each of the four locations containing short wavelength absorptions based on the THEMIS DCS images (Figure 2). For the purpose of this work, we define a surface with short wavelength absorptions as having THEMIS bands 4–5 emissivity equal to or lower than emissivity in bands 7–9. The data were masked based on a maximum band 5 surface emissivity of 0.97. This ensures that surfaces are free of volume scattering effects due to small particle sizes and have sufficient spectral contrast to enable a reliable WAC determination from the silicate Reststrahlen absorption. Spectra with band 5 emissivity values >0.97 typically show the volume scattering feature attributed to dusty surfaces that results in anomalously large WAC values.

The short wavelength absorption surface type has relatively low WAC values. Spectra of surfaces in regions a–d (Figures 2 and 3) have WAC values of 9.28, 9.37, 9.92, and 9.59 μm respectively. By contrast, the surrounding low albedo surfaces in each of these areas typically have larger WAC values of 10.0–10.5 μm. The third surface spectral type has little spectral contrast and, consequently, does not return a reliable WAC determination and is masked out in Figure 2. This low spectral contrast is dominant throughout the region and is consistent with fine-particulate, dusty surfaces that do not contain interpretable Reststrahlen absorptions (e.g., *Ruff and Christensen*, 2002, *Bandfield and Smith*, 2003).

3.1.2 Surface emissivity spectra

THEMIS surface emissivity spectra for the short wavelength absorption surfaces have minimum emissivities of 0.952–0.968 that occur in either THEMIS band 4 or 5 (Figure 3). The emissivity climbs towards longer wavelengths, consistent with the low WAC values of this spectral type. The surrounding low albedo surface spectra have a spectral contrast similar to the short wavelength absorption spectral type, but the minimum occurs in either THEMIS band 5 or 7. In addition, the spectral shape between THEMIS bands 3–9 is more symmetrical, with significantly lower emissivity in THEMIS bands 6–9. The low contrast spectra have relatively low emissivity values in THEMIS bands 1–2 and an additional emissivity minimum in band 8. Bands 3–7 have relatively high emissivity values and a is relatively flat. This spectral type closely matches the spectral response of surface dust (*Bandfield and Smith*, 2003).

3.2 CRISM data

3.2.1 Regional 1.9 μm absorption index images

We inspected CRISM MSP data for 1.9 μm hydration features covering the same region as the THEMIS data. In this case, however, surface coverage is not complete and ranges from ~50–90% within individual regions. Data coverage is less complete in the regions towards the east, primarily because the heavily targeted Nili Fossae region directly to the south required up- and down-track targeting, leaving gaps in the nadir MSP surface coverage. Based on visual inspection, we identified hydration features in numerous locations near the highlands-lowlands boundary, discontinuously spanning ~1200 km from 60.3°E, 33.6°N to 80.6°E, 24.8°N (Figure 4). Exposures are typically within or immediately adjacent to low albedo surfaces near the base of the topographic boundary. We did not identify any exposures near low albedo regions further to the north, east, or west.

We produced detailed 1.9 μm index maps for regions where either hydration spectral features were initially identified in the CRISM data, or THEMIS data indicate the presence of the short wavelength absorption TIR spectral type (Figure 4). Three of the four TIR short wavelength absorption surface type exposures (regions a, c, and d) coincide with the presence of clear 1.9 μm hydration features. Surfaces with the 1.9 μm spectral feature are much more extensive than the TIR high SiO_2 materials. In particular, hydration features appear to be prevalent throughout low albedo exposures in a 450 by 350 km region, centered near 74.5°E, 28.7°N. Unfortunately, this region in particular contains significant gaps in data coverage, making it difficult to estimate the area covered by surfaces containing the hydration features. However, a conservative estimate based on a subjective evaluation of the existing index images indicates coverage of 2675 km^2 for this region and 3474 km^2 for all regions (Figure 4). Hydration spectral features are less common to the northwest and southeast of this region, consistent with the relatively sparse low albedo exposures.

3.2.2 CRISM surface spectra and local scale spectral variations

We examined several CRISM MSP images individually to verify the presence of a 1.9 μm absorption feature indicated by the index images (Figure 5). In addition, each exposure of the TIR short wavelength absorption spectral type was examined using the MSP data (no full spectral resolution data covers these surfaces). In all cases, the presence or absence of a distinct 1.9 μm absorption feature is consistent with the 1.9 μm index maps. There is some indication of the presence of a weak 1.9 μm feature not identified in the index maps, such as within exposure b of the TIR short wavelength absorption type, near 64.9°, 34.1°N. Although the presence of extensive hydration spectral features beyond what is indicated here using the index images is a possibility, it requires additional validation.

Surfaces that have a 1.9 μm hydration feature exhibit a variety of other spectral features. This variety appears in both full spectral resolution and multispectral survey data throughout our region of study. We examined multispectral data west of 70°E that cover surfaces that coincide with high 1.9 μm index values. Full spectral resolution CRISM data are present to the east and are used here to show the spectral diversity in these regions.

We identified two distinct spectral types within the westernmost hydrated surface, near 60.3°E, 33.6°N (near TIR region a; Figure 5). The first spectral type has distinct and relatively narrow absorptions centered near 1.43, 1.93, and 2.30 μm. The 1.43 and 2.30 μm absorptions are weak relative to the 1.93 μm absorption, though still distinct. By contrast, the other spectral type (the green spectrum in Figure 5) has broad and relatively strong absorptions present at 1.43–1.47, 1.93–2.01, and 2.20–2.30 μm. In this case, the 1.43–1.47 and 2.20–2.30 absorptions are prominent, though still only about half the strength of the 1.93–2.01 μm absorption. As described above, there is some indication that surfaces with a weak 1.9 μm absorption are present elsewhere in the region, suggesting that the presence of hydrated phases may be more widespread (Figure 5). The limited spectral sampling of the CRISM multispectral survey data prevents the precise identification of absorption wavelength minima, making the identification of specific phases more difficult.

The presence of full spectral resolution CRISM data covering hydrated surfaces to the east allows for a more detailed analysis. We focus here on three images, centered near 73.3°E, 29.3°N, 76.6°E, 27.8°N, and 80.4°E, 24.8°N (labeled NIR examples 1–3 and near TIR regions c and d), which sample much of the geographical extent of the hydrated exposures. The full spectral resolution CRISM images provide more detailed examples of the spectral variety identified within the hydrated regions we mapped using the low spectral resolution MSP data. This analysis provides only a sampling of the spectral character of the hydrated surfaces and is not meant to be comprehensive.

There appear to be four main hydrated spectral types based on the analysis of the CRISM data (Figure 6): 1) a less pervasive surface type containing ~1.4, 1.93, and broad 2.20–2.30 μm absorptions, 2) a spatially pervasive surface type with 1.43, 1.93, and 2.29 μm absorptions of variable strength, 3) an isolated spectral type with broad 2.30 and 2.50 μm absorptions, and 4) a spectral type containing only the hydration absorption centered near 1.93 μm. It is possible that there are additional hydrated spectra present in the region and spectral variability within these defined spectral types. Regardless, these four spectral types encompass most of the spectral diversity identified throughout the region.

The westernmost image (NIR example 1) contains two hydrated spectral types. In both cases, we identified a prominent absorption, centered near 1.93 μm, with little variation in band position or shape. Over many areas, there are additional spectral absorptions of variable strength centered near 1.43 and 2.29 μm. However, over other surfaces, the 2.29 μm absorption is absent (Figure 7) and the 1.43 μm feature is subdued.

Three hydrated spectral types are present in the region centered near 76.6°E, 27.8°N (NIR example 2). Similar to the western region, we identified a widespread spectral type with 1.93, 2.29, and weak 1.43 μm absorptions. Two other hydrated spectral types are present, though their geographical extent is more limited (Figure 8). One spectral type contains absorptions with minima near 1.38 and 2.20 μm. The 2.20 μm absorption is broad and asymmetrical, bearing some similarity to the spectral type to the west defined using the multispectral data. An additional isolated spectral type has two relatively broad absorptions with minima centered near 2.30 and 2.50 μm (Figure 6).

The easternmost image (NIR example 3) shows two spectral types, similar to the western image. Again, in both cases, a prominent absorption centered near 1.93 μm is present, although in this case, there appears to be some variability in band shape. However, this variability may not reflect surface compositional variations because this spectral region may have a higher uncertainty due to residual effects of a prominent atmospheric water vapor absorption. We identified additional spectral absorptions of variable strength, including a weak 1.43 absorption and a distinct and 2.29 μm absorption. Over isolated surfaces, these features are absent (Figure 9), though there is some suggestion of a weak, broad 2.20-2.30 μm absorption.

3.3 Morphological properties

3.3.1 *Regional Setting*

All high bulk SiO_2 and hydrated surface exposures in the region are located near or at the base of topographic scarps within the zone of transition between the southern highlands and northern lowlands. In addition, exposures are within or adjacent to low albedo surfaces are dominated by duneforms. Although similar regional settings with layered sediments, low albedo terrains, and topographic scarps are present at other locations across the dichotomy boundary, we did not identify any other significant exposures of high Si or hydrated phases at the base of highly fractured terrain. Mars Orbiter Laser Altimeter (MOLA; *Smith et al.*, 2001) elevation data indicate the high bulk SiO_2 and hydrated surface exposures occur over a range of relatively low elevations (Figure 1). For example, the four high bulk SiO_2 sites span elevations from -3100 to -1800 m.

Topographic knobs that appear to be more isolated islands of the highly fractured terrain are also associated with adjacent low albedo surfaces. These knobs are present further within the northern lowlands and these surfaces also lack any spectral evidence of high Si or hydrated phases. In summary, we find that the high SiO_2 and hydrated surface types are contained within the Nilosyrtis Mensae region adjacent to the dichotomy boundary. Other surfaces outside this region with a similar geological context are present along the dichotomy boundary and within the northern lowlands. However, these surfaces do not show evidence for either high bulk SiO_2 contents or hydrated phases.

3.3.2 *THEMIS High SiO_2 Surfaces*

CTX images are available that cover the four high SiO_2 surfaces identified using THEMIS data. In all cases, the high bulk SiO_2 surfaces appear smooth and relatively featureless with an intermediate albedo relative to adjacent surfaces (Figure 10). Low albedo dune forms are present near the surfaces of interest and, in some cases, light-toned ripple forms are present within the high SiO_2 surface types. The high SiO_2 surfaces are typically adjacent to, but not within, surface morphological units that appear rough and somewhat dissected in the CTX images. In addition, although the high SiO_2 surfaces do not appear layered, layering is present nearby in each region.

3.3.3 *CRISM Hydrated Surfaces*

A variety of morphological surface types are associated with the four CRISM spectral types.

Surfaces containing absorptions near 2.29 μm appear relatively light-toned and are heavily fractured to the limit of the spatial resolution, typically with numerous boulders present. This material can appear coarsely layered within a larger sequence of other hydrated materials (Figure 11). We observe a similar surface texture and morphology for the isolated area that contains broad 2.3 and 2.5 μm absorptions (Figure 11).

Surfaces that have a 1.9 μm absorption, but lack other distinctive spectral features and do not show a consistent surface morphology. We find that these surfaces can be finely layered, smooth and featureless, or with pervasive jointing (Figure 12). The spectral type containing broader absorptions near 1.4, 1.9, and 2.2–2.3 μm, shows a morphology similar to the high SiO_2 TIR spectral type. It is relatively featureless with a moderate albedo relative to the surrounding terrain. There is some faint indication of layering and fractures, but these are much more prominent in the immediately surrounding terrain (Figure 12).

4. Discussion

4.1 Surface Compositions

The THEMIS data show short wavelength absorptions within the regions shown in Figure 1. These surfaces appear to be dominated by high Si phases, based on visual comparison and the low WAC values (Figures 2 and 3). Similar spectral shapes and WAC values have been identified only in a few instances elsewhere on Mars, including western Hellas Basin (e.g., *Bandfield*, 2008; *Bandfield et al.*, 2013), near Antoniadi Crater (e.g., *Bandfield,* 2006; *Smith and Bandfield*, 2012), and at Gusev Crater (*Ruff et al.*, 2011). These regions are large enough for higher spectral resolution TES data (or, in the case of Gusev Crater, Mini-TES observations from the Mars Exploration Rover) to confidently identify high concentrations of quartz and/or poorly crystalline silica. CRISM data have been used to identify the presence of opaline silica in both of these regions, consistent with a high bulk SiO_2 content (*Ehlmann et al.*, 2009; *Smith and Bandfield,* 2012; *Bandfield et al.*, 2013). Although the THEMIS data do not have the spectral resolution required to determine the precise mineralogy, we find that the short wavelength absorptions, corresponding low WAC values, and the spectral similarity to other high SiO_2 surfaces indicates that this is another region where surfaces are dominated by high Si phases (Figure 13).

The high bulk SiO_2 surfaces in Nilosyrtis Mensae are nearly identical in spectral shape to those of the high bulk SiO_2 surfaces in western Hellas Basin and the ~8–12 μm silicate absorption is concentrated at significantly shorter wavelengths than other surfaces with high bulk SiO_2 contents

(Figure 13). This is reflected in the WAC values of martian high SiO_2 spectral types. The average Nilosyrtis Mensae high SiO_2 surface spectrum (excluding the second easternmost exposure, which is somewhat subdued relative to the others) has a WAC value of 9.33 µm, close to that of western Hellas Basin (9.27 µm; *Bandfield*, 2008) and significantly lower than Antoniadi Crater (9.71 µm; *Bandfield*, 2006), Nili Patera Caldera (9.86 µm; *Christensen et al.*, 2005) and the global Surface Type 2 high SiO_2 surface (9.96 µm; *Bandfield et al.*, 2000). The low WAC values in Nilosyrtis Mensae are consistent with a composition dominated by high Si phases (*Smith et al.*, 2013) such as the surfaces containing nearly 80% amorphous silica concentrations identified in western Hellas Basin (*Bandfield*, 2008). By contrast, *Rogers and Nekvasil* (2015) use a similar method with THEMIS data to show the lack of high SiO_2 surfaces at other locations.

CRISM multispectral data over the high SiO_2 sites shows spectral variability that appears spatially independent of the TIR data. In three of the high bulk SiO_2 regions, there is a 1.9 µm hydration feature, whereas we do not confidently detect this feature in TIR region c. Although this lack of correlation between datasets can be perplexing, it bears some similarity to other regions on Mars (e.g., *Michalski et al.*, 2013; *Viviano and Moersch*, 2013). Part of the discrepancy might be explained by the different sensitivities of the two datasets. The NIR spectral data is especially sensitive to hydrated phases at small particle sizes and the TIR data is more broadly sensitive to bulk mineralogy, especially at particle sizes >~100 µm. In addition, it is possible that quartz is present within the high bulk SiO_2 surfaces, which may not be detected in the NIR datasets if it is not hydrated.

Hydrated phases are isolated but widespread in CRISM data and do appear to be at least regionally associated with the TIR high SiO_2 surface types (Figure 4). The CRISM MSP hydration index map provides an indication of the extent of the hydrated materials, regardless of their specific phase. The relatively vast and extensive nature of the hydrated phases indicates that any associated aqueous alteration was a regional process and not limited to isolated locations. Even by itself, the region covering 72–78°E, 26–31°N (containing TIR region c and NIR examples 1 and 2) spans an area ~300 by 150 km and is one of the largest surface exposures of hydrated silicates on the planet (*Poulet et al.*, 2008).

Although coverage is limited, the full spectral resolution CRISM data can provide detailed snapshots of the specific hydrated phases and their relationship with surface morphology and textures. Most surfaces have an associated broad 2.2–2.3 µm absorption or, more commonly, a narrow absorption centered near 2.29 µm (Figure 5). These two spectral shapes are consistent with Si-OH and (Fe,Mg)-OH vibrational absorptions respectively, such as those present in hydrated silica (e.g., *Rice et* *al.*, 2013; *Smith et al.*, 2013) and Fe/Mg-smectites, which have been previously identified in the region (*Poulet et al.*, 2008; *Ehlmann et al.*, 2009). Other surfaces have a distinct 1.9 μm absorption without clear evidence for other absorption features. However, in these cases, the 1.9 μm absorption is relatively weak and we think it is plausible that weaker absorptions near 1.4 and 2.2–2.3 μm are present, but simply not detected. This includes the potential presence of zeolites with an absorption near 2.5 μm. It is important to remember that the spectra shown in Figures 5 and 6 are ratios that may also be canceling out other spectral features. Finally, spectra from one isolated region have absorptions with minima near 1.93, 2.31, and 2.51 μm, consistent with Mg-carbonates identified in the Nili Fossae and Syrtis Major regions to the south (e.g., *Ehlmann et al.*, 2008; *Ehlmann et al.*, 2009).

In general, the hydrated compositions identified in the NIR spectral data are similar to those identified elsewhere on Mars, especially in the Antoniadi Crater, Syrtis Major, and Nili Fossae regions immediately to the south (e.g., *Ehlmann et al.*, 2009; *Mustard et al.*, 2009; *Smith and Bandfield*, 2012). However, the compositional range appears somewhat limited compared to other regions containing evidence for extensive aqueous alteration. For example, there appears to be a greater diversity of aqueous phases in the Nili Fossae and Mawrth Vallis regions (e.g., *Ehlmann et al.*, 2009; *Bishop et al.*, 2008). By contrast, there is evidence for extensive aqueous alteration in western Hellas Basin, but the region only shows evidence for hydrated silica (*Bandfield et al.*, 2013) and potentially zeolites (*Carter et al.*, 2013).

Many surfaces that show evidence for hydrated phases in CRISM data have spectral signatures consistent with a basaltic composition in THEMIS data (Figure 3). Although NIR datasets have been used to identify many sites containing high Si alteration phases, such as phyllosilicates (e.g., *Poulet et al.*, 2005), many of these locations are dominated by primary mafic phases based on analysis of TIR datasets (e.g., *Rogers*, 2011). This illustrates the complementary sensitivities of the two wavelength regions; small amounts of hydrated alteration products can be readily detected at NIR wavelengths, whereas TIR measurements are dominated by the bulk composition (plagioclase and pyroxene in this case).

4.2 Geological Context

The hydrated and high bulk SiO_2 surfaces are near the base of the topographic scarp that delineates the hemispheric dichotomy boundary (Figure 1). Regions with a similar geomorphological context exist elsewhere along this topographic boundary and at isolated locations within the northern lowlands. However, in both of these cases, we find no evidence for similar hydrated or high SiO_2 materials. One possible exception may be Fe/Mg-smectites and hydrated silica identified in Acidalia Planitia

(*Ehlmann et al.*, 2011; *Carter et al.*, 2013; *Pan and Ehlmann*, 2014). However, these compositions are associated with km-scale cone-shaped features and are not immediately adjacent to the hemispheric boundary and do not appear to be remnant highlands terrains.

Both the hydrated and high SiO_2 surfaces are associated regionally with low albedo (<0.15) surfaces but, based on our examination of high resolution images, these compositions are not necessarily dark toned themselves. Similar to western Hellas Basin, sand appears to be scouring nearby surfaces free of mantling dust. The Nilosyrtis Mensae region is one of several large scale albedo features on Mars that has changed significantly aver annual and decadal timescales, indicating the presence of a widespread but thin veneer of dust (*Geissler*, 2005). This thin layer appears to be cleared away in many regions, offering a unobscured view of the underlying rocks. The surface materials appear smooth and featureless to highly fractured with numerous rocks visible (Figures 10–12). Layering is typically present and the high bulk SiO_2 and hydrated materials are within what appear to be partially exhumed sediments that were shed off the adjacent highlands and topographic knobs. In some cases, these sediments may simply slough off an adjacent topographic scarp. There are also numerous valleys in the region that appear to have been carved by water and/or ice, which would transport sediments to the low lying areas at some distance from the source.

The layering and fractured nature of the materials indicates that they are bedrock and not currently mobile sediments. However, the friable nature of the materials in many locations and the overall moderate thermal inertia values in the region (data from the Thermal Emission Spectrometer show values of ~150–450 $J\ m^{-2}\ K^{-1}\ s^{-½}$) indicate that the materials are poorly consolidated and not consistent with the presence of high strength blocks or bedrock. In general, we conclude that the high bulk SiO_2 and hydrated materials appear to be weakly cemented sand- and siltstones that are sourced from adjacent and nearby highlands terrains.

We are assuming here that the high SiO_2 materials are formed by aqueous processes, and are not primary igneous materials. The presence of these materials within poorly consolidated layered sediments indicates that they have been reworked significantly from any potential igneous origin. In addition, in many cases, the high SiO_2 materials coincide with hydration features present in the CRISM data, indicating the presence of alteration. Finally, the extremely high concentration of high Si phases necessary to produce the spectral signature here would require an igneous composition higher in SiO_2 than identified elsewhere on the planet. For comparison, TIR data covering high Si compositions near Antoniadi crater proposed to be of granitic origin (Bandfield, 2006) have significantly lower WAC values and a spectral shape with longer wavelength absorptions (Figure 13).

It is not clear if the alteration and aqueous conditions occurred prior to, or after the sediments were deposited. We do not see any evidence for aqueous phases in the walls of the immediately adjacent remnant scarps. However, these surfaces may remain mantled by dust and similar alteration and high Si phases are found in the highlands terrains further to the south (e.g., *Ehlmann et al.*, 2009; *Mustard et al.*, 2009; *Smith and Bandfield*, 2012). This indicates that, at least regionally, aqueously altered source materials are present in the bedrock and may have been a sediment source for the low lying areas.

We postulate that the high bulk SiO_2 and hydrated materials form by an aqueous process that was consistently present throughout the region. In that sense, we are linking them together as the focus of this work. It is likely that additional materials are present, but not exposed throughout the region. This is based on the fact that most exposures are within or adjacent to the sands that are likely scouring the surface free of mantling dust. However, we do not have evidence that the high SiO_2 and hydrated materials form one contiguous unit across ~1200 km of the dichotomy boundary.

4.3 Formation Conditions

The dominance of hydrated silica and Fe/Mg-smectites in the NIR data indicates relatively light amounts of alteration at low temperatures. This is consistent with many other locations on Mars with evidence for aqueous alteration. With enough exposure to water at high enough temperatures, hydrated silica and Fe/Mg-smectites will undergo diagenesis and transform to quartz and illite respectively (e.g., *Tosca and Knoll*, 2009). For example, Tosca and Knoll (2009) estimate complete conversion of opal-CT to quartz exposed to water at 273 K in 300–400 Ma. However, this duration is likely an overestimate, especially at elevated temperatures, and opaline silica is rarely found on Earth in rocks more than a few million years old (*Tosca and Knoll*, 2009). Although smectites and hydrated silica phases have been identified in many locations (e.g., *Murchie et al.*, 2009), only limited exposures of quartz and perhaps illite have been identified (*Bandfield*, 2006; *Mustard et al.*, 2008; *Smith and Bandfield*, 2012).In this sense, we believe the exposure of materials to water in the Nilosyrtis Mensae region has been limited in temperature and/or duration.

The hydrated and high bulk SiO_2 materials indicate the presence of widespread water in large quantities, even though the temperature and duration of exposure may have been limited. Although the high SiO_2 materials are spatially limited, they occur over a large region and may be isolated windows into more extensive exposures that are mantled with aeolian sediments. Large water to rock ratios are required to form such high concentrations of Si-rich phases and separate them from the iron, magnesium, and calcium that were presumably present in significant quantities in the unaltered source material. For example, a concentration of 80 vol. % hydrated silica is consistent with the high SiO_2

exposures detected using THEMIS data, similar to hydrated silica deposits in western Hellas Basin. As a rough estimate, assuming silica saturated water at 298K (115 ppm; *Morey et al.*, 1964), ~8700 kg of saturated water is necessary to carry and precipitate 1 kg of opaline silica. Of course, these values can be highly variable based on environmental factors such as pH and temperature, but in most cases a substantial amount of water is required to form such high concentrations of silica (e.g., *McAdam et al.*, 2009).

The hydrated exposures identified using CRISM data are more continuous and cover a much larger total area (Figures 1 and 4), but appear to be present in lower concentrations (likely <10–15 areal %) based on the dominance of its basaltic spectral signature in the TIR data. Despite these low concentrations, the widespread coverage of the hydrated materials requires a widely distributed source of water, even if present for a limited time and at relatively low water to rock ratios.

What is the source of the water? The presence of the aqueous materials within the northern lowlands could be related to the presence of a large body of water postulated to have been present in martian history (e.g., *Carr and Head*, 2003). However, if this body of water is responsible for the aqueous alteration products, we would expect to see additional widespread alteration products elsewhere along the dichotomy boundary, as well as further within the northern lowlands where “islands” of remnant terrain exist such as areas to the north and east of the dichotomy boundary (Figure 2). A different potential source of water may be the same that carved the valleys and channels that are common at the dichotomy boundary. Once again, we find that this is inconsistent with the lack of alteration products present in a similar geologic and geomorphic context at many other locations along the dichotomy boundary.

The altered materials may have instead been formed within the highlands crust to the south and then deposited in their current location. Even though this transport and deposition likely required some amount of liquid water, it may not have played a significant role in the production of the previously altered materials. The numerous valleys in the region are evidence for a source of both groundwater and sediments from the altered crust to the south. This would explain the presence of the extensive aqueous compositions within this limited stretch of the dichotomy boundary and why these compositions are not more common within the lowlands in general, which might be the case if they were formed in situ. In addition, the similarities in alteration products identified in the adjacent highlands is consistent with those we identified in Nilosyrtis Mensae. In this sense, the high bulk SiO_2 and hydrated compositions present in the lowlands in Nilosyrtis Mensae may have formed from a silica-saturated groundwater and/or direct transport of pre-existing altered materials. In either case, these materials may represent an extensive and well-exposed sampling of crustal aqueous processes throughout the region. Although not contiguous, the widespread nature of the high SiO_2 and hydrated materials throughout indicate that this process was common throughout Nilosyrtis Mensae at the dichotomy boundary.

4.4 Relationship to Other Regions

We are grouping these exposures of high SiO_2 and hydrated materials as a single entity that is separate from other exposures of aqueous compositions on Mars, based on the similarities in composition, surface morphology, and geologic context. Although this may not be classified as a continuous geologic unit, it may represent a similar set of formation processes during a particular epoch in martian history. However, as described above, these materials may be sourced from the highlands crust to the south. Indeed, the southeast extent of the region of interest is not well-separated from the Nili Fossae region, which has been well-studied and remains a location of intense interest (e.g., *Hamilton and Christensen*, 2005; *Mustard et al.*, 2009). In this region, aqueous phases are clearly present in both valley floors and within exposures of bedrock at higher elevations (*Mustard et al.*, 2009).

Although geographically well-separated, the high bulk SiO_2 and hydrated deposits are similar to the aqueous compositions identified within western Hellas Basin (*Bandfield*, 2008; *Bandfield et al.*, 2013). In both cases, smooth and relatively featureless layered materials are dominated by high SiO_2 phases in TIR data. The materials are present across a wide region at the base of a topographic scarp with evidence for sediment deposition and a widespread groundwater source. In the case of Hellas Basin, NIR spectral data only shows evidence for hydrated silica and potentially zeolites (*Bandfield et al.*, 2013; *Carter et al.*, 2013), in contrast to the hydrated silica and Fe,Mg smectites identified in the Nilosyrtis Mensae region. In both cases, the aqueous compositions may be the result of a widespread source of groundwater that intersected the surface at a large topographic scarp.

5. Conclusions

We have identified widespread exposures of high bulk SiO_2 and hydrated compositions throughout the Nilosyrtis Mensae region. These compositions are typically present within sediments at the base of the topographic scarp that delineates the global dichotomy boundary. Although the hydrated and high SiO_2 compositions are not always coincident and the hydrated compositions are much more extensive, they appear to be related. The materials may have formed from groundwater discharge and transport of altered compositions found throughout the crust in the Syrtis Major and Nili Fossae regions to the south. This is one of the most extensive exposures of altered compositions identified to date on Mars. High bulk SiO_2 and hydrated compositions are found in a similar geomorphological context in western Hellas Basin. The Nilosyrtis Mensae and western Hellas Basin regions may both have compositions that reflect aqueous conditions within the adjacent crust of the martian highlands.

Acknowledgments

We would like to thank the Mars Odyssey and Mars Reconnaissance Orbiter operations teams for targeting, collecting, and archiving the various datasets used here. JMARS, Davinci, ISIS, and GDAL software was used for data processing and analysis. Vicky Hamilton and an anonymous reviewer provided detailed comments that greatly improved both the clarity and quality of this work. Funding for this project was provided in part by the 2001 Mars Odyssey project and Mars Data Analysis Program grant NNX14AM33G.

References

Amador, E. S. and J. L. Bandfield (2015) Localized Alteration of the Capping Unit in Nili Fossae, Mars: Evidence for Multiple Episodes of Aqueous Alteration. Lunar and Planetary Science Conference, 46, 1189.

Bandfield, J. L. (2008) High-silica deposits of an aqueous origin in western Hellas Basin, Mars. Geophysical Research Letters, *35*, 1220510.1029/2008GL033807.

Bandfield, J. L. (2006) Extended surface exposures of granitoid compositions in Syrtis Major, Mars. Geophysical Research Letters, 33, L0620310.1029/2005GL025559.

Bandfield, J. L. and M. D. Smith (2003) Multiple emission angle surface-atmosphere separations of Thermal Emission Spectrometer data. Icarus, 161, 47-65 10.1016/S0019-1035(02)00025-8.

Bandfield, J. L., E. S. Amador, and N. H. Thomas (2013) Extensive hydrated silica materials in western Hellas Basin, Mars. Icarus, 226, 1489-1498 10.1016/j.icarus.2013.08.005.

Bandfield, J. L., D. Rogers, M. D. Smith, and P. R. Christensen (2004a) Atmospheric correction and surface spectral unit mapping using Thermal Emission Imaging System data. Journal of Geophysical Research, *109*, 1000810.1029/2004JE002289.

Bandfield, J. L., V. E. Hamilton, P. R. Christensen, and H. Y. McSween (2004b) Identification of quartzofeldspathic materials on Mars. Journal of Geophysical Research, *109*, 1000910.1029/2004JE002290.

Bandfield, J. L., T. D. Glotch, and P. R. Christensen (2003) Spectroscopic Identification of Carbonate Minerals in the Martian Dust. Science, *301*, 1084-1087 10.1126/science.1088054.

Bandfield, J. L., V. E. Hamilton, and P. R. Christensen (2000) A Global View of Martian Surface Compositions from MGS-TES. Science, *287*, 1626-1630 10.1126/science.287.5458.1626.

Barnhart, C. J. and F. Nimmo (2011) Role of impact excavation in distributing clays over Noachian surfaces. Journal of Geophysical Research, 116, E0100910.1029/2010JE003629.

Bishop, J. L., and 11 colleagues (2008) Phyllosilicate Diversity and Past Aqueous Activity Revealed at Mawrth Vallis, Mars. Science, *321*, 83010.1126/science.1159699.

Carr, M. H. and J. W. Head (2003) Oceans on Mars: An assessment of the observational evidence and possible fate. Journal of Geophysical Research, 108, 504210.1029/2002JE001963.

Carter, J., F. Poulet, J.-P. Bibring, N. Mangold, and S. Murchie (2013) Hydrous minerals on Mars as seen by the CRISM and OMEGA imaging spectrometers: Updated global view. Journal of Geophysical Research (Planets), 118, 831-858, 10.1029/2012JE004145.

Christensen, P. R., and 10 colleagues (2004) The Thermal Emission Imaging System (THEMIS) for the Mars 2001 Odyssey Mission. Space Science Reviews, *110*, 85-130 10.1023/B:SPAC.0000021008.16305.94.

Christensen, P. R., R. V. Morris, M. D. Lane, J. L. Bandfield, and M. C. Malin (2001) Global mapping of Martian hematite mineral deposits: Remnants of water-driven processes on early Mars. Journal of Geophysical Research, *106*, 23873-23886 10.1029/2000JE001415.

Edwards, C. S., K. J. Nowicki, P. R. Christensen, J. Hill, N. Gorelick, and K. Murray (2011) Mosaicking of global planetary image datasets: 1. Techniques and data processing for Thermal Emission Imaging System (THEMIS) multi-spectral data. Journal of Geophysical Research, *116*, 1000810.1029/2010JE003755.

Ehlmann, B. L., J. F. Mustard, S. L. Murchie, J.-P. Bibring, A. Meunier, A. A. Fraeman, and Y. Langevin (2011) Subsurface water and clay mineral formation during the early history of Mars. Nature, 479, 53-60, 10.1038/nature10582.

Ehlmann, B. L., and 11 colleagues (2009) Identification of hydrated silicate minerals on Mars using MRO-CRISM: Geologic context near Nili Fossae and implications for aqueous alteration. Journal of Geophysical Research, *114*, 010.1029/2009JE003339.

Ehlmann, B. L., and 13 colleagues (2008) Orbital Identification of Carbonate-Bearing Rocks on Mars. Science, *322*, 182810.1126/science.1164759.

Farrand, W. H., T. D. Glotch, J. W. Rice, J. A. Hurowitz, and G. A. Swayze (2009) Discovery of jarosite within the Mawrth Vallis region of Mars: Implications for the geologic history of the region. Icarus, 204, 478-488, 10.1016/j.icarus.2009.07.014.

Geissler, P. E. (2005) Three decades of Martian surface changes. Journal of Geophysical Research, 110, E0200110.1029/2004JE002345.

Gendrin, A., and 10 colleagues (2005) Sulfates in Martian Layered Terrains: The OMEGA/Mars Express View. Science, *307*, 1587-1591 10.1126/science.1109087.

Gillespie, A. R., A. B. Kahle, and R. E. Walker (1986) Color enhancement of highly correlated images: I. Decorrelation and HIS contrast stretches, Remote Sensing of Environment, *20*, 209– 235.

Hamilton, V. E. and P. R. Christensen (2005) Evidence for extensive, olivine-rich bedrock on Mars. Geology, 33, 43310.1130/G21258.1.

Hamilton, V. E., P. R. Christensen, H. Y. McSween Jr., and J. L. Bandfield (2003) Searching for the source regions of martian meteorites using MGS TES: Integrating martian meteorites into the global distribution of igneous materials on Mars. Meteoritics and Planetary Science, 38, 871-885 10.1111/j.1945-5100.2003.tb00284.x.

Hoefen, T. M., R. N. Clark, J. L. Bandfield, M. D. Smith, J. C. Pearl, and P. R. Christensen (2003) Discovery of Olivine in the Nili Fossae Region of Mars. Science, 302, 627-630 10.1126/science.1089647.

Loizeau, D., N. Mangold, F. Poulet, J.-P. Bibring, A. Gendrin, V. Ansan, C. Gomez, B. Gondet, Y. Langevin, P. Masson, and G. Neukum (2007) Phyllosilicates in the Mawrth Vallis region of Mars. Journal of Geophysical Research, 112, E08S0810.1029/2006JE002877.

Malin, M. C., J. F. Bell, B. A. Cantor, M. A. Caplinger, W. M. Calvin, R. T. Clancy, K. S. Edgett, L. Edwards, R. M. Haberle, P. B. James, S. W. Lee, M. A. Ravine, P. C. Thomas, and M. J. Wolff (2007) Context Camera Investigation on board the Mars Reconnaissance Orbiter. Journal of Geophysical Research, 112, E05S0410.1029/2006JE002808.

McAdam, A. C., M. Y. Zolotov, M. V. Mironenko, and T. G. Sharp (2008) Formation of silica by low-temperature acid alteration of Martian rocks: Physical-chemical constraints. Journal of Geophysical Research (Planets), 113, E0800310.1029/2007JE003056.

McEwen, A. S., and 14 colleagues (2007) Mars Reconnaissance Orbiter's High Resolution Imaging Science Experiment (HiRISE). Journal of Geophysical Research, *112*, 510.1029/2005JE002605.

McGuire, P. C., and 14 colleagues (2009) An improvement to the volcano-scan algorithm for atmospheric correction of CRISM and OMEGA spectral data. Planetary and Space Science, *57*, 809-815 10.1016/j.pss.2009.03.007.

McKeown, N. K., J. L. Bishop, E. Z. Noe Dobrea, B. L. Ehlmann, M. Parente, J. F. Mustard, S. L. Murchie, G. A. Swayze, J.-P. Bibring, and E. A. Silver (2009) Characterization of phyllosilicates observed in the central Mawrth Vallis region, Mars, their potential formational processes, and implications for past climate. Journal of Geophysical Research, 114, E00D1010.1029/2008JE003301.

Michalski, J. R., P. B. Niles, J. Cuadros, and A. M. Baldridge (2013) Multiple working hypotheses for the formation of compositional stratigraphy on Mars: Insights from the Mawrth Vallis region. Icarus, 226, 816-840, 10.1016/j.icarus.2013.05.024.

Milliken, R. E., and 11 colleagues (2008) Opaline silica in young deposits on Mars. Geology, *36*, 847-850, 10.1130/G24967A.1.

Morey, G. W., R. O. Fournier, and J. J. Rowe (1964) The Solubility of Amorphous Silica at 25°C. Journal of Geophysical Research, 69, 1995-2002, 10.1029/JZ069i010p01995.

Morris, R. V., S. W. Ruff, R. Gellert, D. W. Ming, R. E. Arvidson, B. C. Clark, D. C. Golden, K. Siebach, G. Klingelhöfer, C. Schröder, I. Fleischer, A. S. Yen, and S. W. Squyres (2010) Identification of Carbonate-Rich Outcrops on Mars by the Spirit Rover. Science, 329, 42110.1126/science.1189667.

Murchie, S. L., and 22 colleagues (2009) Compact Reconnaissance Imaging Spectrometer for Mars investigation and data set from the Mars Reconnaissance Orbiter's primary science phase. Journal of Geophysical Research, 114, 010.1029/2009JE003344.

Murchie, S., and 49 colleagues (2007) Compact Reconnaissance Imaging Spectrometer for Mars (CRISM) on Mars Reconnaissance Orbiter (MRO). Journal of Geophysical Research, *112*, 510.1029/2006JE002682.

Mustard, J. F., B. L. Ehlmann, S. L. Murchie, F. Poulet, N. Mangold, J. W. Head, J.-P. Bibring, and L. H. Roach (2009), Composition, Morphology, and Stratigraphy of Noachian Crust around the Isidis basin, Journal of Geophysical Research, *114*, 10.1029/2009JE003349.

Mustard, J. F., and 35 colleagues (2008) Hydrated silicate minerals on Mars observed by the Mars Reconnaissance Orbiter CRISM instrument. Nature, 454, 305-309 10.1038/nature07097.

Noe Dobrea, E. Z., J. L. Bishop, N. K. McKeown, R. Fu, C. M. Rossi, J. R. Michalski, C. Heinlein, V. Hanus, F. Poulet, R. J. F. Mustard, S. Murchie, A. S. McEwen, G. Swayze, J.-P. Bibring, E. Malaret, and C. Hash (2010) Mineralogy and stratigraphy of phyllosilicate-bearing and dark mantling units in the greater Mawrth Vallis/west Arabia Terra area: Constraints on geological origin. Journal of Geophysical Research, 115, E00D1910.1029/2009JE003351.

Osterloo, M. M., V. E. Hamilton, J. L. Bandfield, T. D. Glotch, A. M. Baldridge, P. R. Christensen, L. L. Tornabene, and F. S. Anderson (2008) Chloride-Bearing Materials in the Southern Highlands of Mars. Science, *319*, 165110.1126/science.1150690.

Pan, C., A. D. Rogers, and J. R. Michalski (2015) Thermal and near-infrared analyses of central peaks of Martian impact craters: Evidence for a heterogeneous Martian crust. Journal of Geophysical Research, 120, 662-688, 10.1002/2014JE004676.

Pan, L. and B. L. Ehlmann (2014) Phyllosilicate and hydrated silica detections in the knobby terrains of Acidalia Planitia, northern plains, Mars. Geophysical Research Letters, 41, 1890-1898

10.1002/2014GL059423.

Pelkey, S. M., and 11 colleagues (2007) CRISM multispectral summary products: Parameterizing mineral diversity on Mars from reflectance. Journal of Geophysical Research, *112*, 810.1029/2006JE002831.

Poulet, F., J. Carter, J. L. Bishop, D. Loizeau, and S. M. Murchie (2014) Mineral abundances at the final four curiosity study sites and implications for their formation. Icarus, 231, 65-76 10.1016/j.icarus.2013.11.023.

Poulet, F., J.-P. Bibring, J. Carter, Y. Langevin, N. Mangold, J. Mustard, D. Loizeau, and B. Gondet (2008) Identification, Mapping and Mineralogy of Phyllosilicates on Mars as Seen by MEx/OMEGA. LPI Contributions, 1441, 68

Poulet, F., J.-P. Bibring, J. F. Mustard, A. Gendrin, N. Mangold, Y. Langevin, R. E. Arvidson, B. Gondet, and C. Gomez (2005) Phyllosilicates on Mars and implications for early martian climate. Nature, *438*, 623-627 10.1038/nature04274.

Rice, M.S., E.A. Cloutis, J.F. Bell III, D.L. Bish, B.H. Horgan, S.A. Mertzman, M.A. Craig, R.W. Renaut, B. Gautason, B. Mountain (2013) Reflectance Spectra Diversity of Silica-Rich Materials: Sensitivity to Environment and Implications for Detections on Mars, Icarus, *223*, 10.1016/j.icarus.2012.09.021.

Rogers, A. D. (2011) Crustal compositions exposed by impact craters in the Tyrrhena Terra region of Mars: Considerations for Noachian environments. Earth and Planetary Science Letters, 301, 353-364 10.1016/j.epsl.2010.11.020.

Rogers, A. D. and H. Nekvasil (2015) Feldspathic rocks on Mars: Compositional constraints from infrared spectroscopy and possible formation mechanisms. Geophysical Research Letters, 42, 2619-2626, 10.1002/2015GL063501.

Rogers, A. D., P. R. Christensen, and J. L. Bandfield (2005) Compositional heterogeneity of the ancient Martian crust: Analysis of Ares Vallis bedrock with THEMIS and TES data. Journal of Geophysical Research, 110, E0501010.1029/2005JE002399.

Ruff, S. W. and P. R. Christensen (2002) Bright and dark regions on Mars: Particle size and mineralogical characteristics based on Thermal Emission Spectrometer data. Journal of Geophysical Research, 107, 512710.1029/2001JE001580.

Ruff, S. W., and 10 colleagues (2011) Characteristics, distribution, origin, and significance of opaline silica observed by the Spirit rover in Gusev crater, Mars. Journal of Geophysical Research, *116*, 010.1029/2010JE003767.

Smith, D. E., and 23 colleagues (2001) Mars Orbiter Laser Altimeter: Experiment summary after the first year of global mapping of Mars. Journal of Geophysical Research, 106, 23689-23722 10.1029/2000JE001364.

Smith, M. R., and J. L. Bandfield (2012) Geology of quartz and hydrated silica-bearing deposits near Antoniadi Crater, Mars. Journal of Geophysical Research, *117*, 600710.1029/2011JE004038.

Smith, M. R., J. L. Bandfield, E. A. Cloutis, and M. S. Rice (2013) Hydrated silica on Mars: Combined analysis with near-infrared and thermal-infrared spectroscopy. Icarus, 223, 633-648 10.1016/j.icarus.2013.01.024.

Tosca, N. J. and A. H. Knoll (2009) Juvenile chemical sediments and the long term persistence of water at the surface of Mars. Earth and Planetary Science Letters, *286*, 379-386 10.1016/j.epsl.2009.07.004.

Vincent, R. K. and F. Thomson (1972) Spectral compositional imaging of silicate rocks. Journal of Geophysical Research, 77, 2465-2472, 10.1029/JB077i014p02465.

Viviano, C. E. and J. E. Moersch (2013) Using THEMIS data to resolve the discrepancy between CRISM/OMEGA and TES modeled phyllosilicate abundance in Mawrth Vallis. Icarus, 226, 497-509 10.1016/j.icarus.2013.06.005.

Viviano, C. E., J. E. Moersch, and H. Y. McSween (2013) Implications for early hydrothermal environments on Mars through the spectral evidence for carbonation and chloritization reactions in the Nili Fossae region. Journal of Geophysical Research (Planets), 118, 1858-1872, 10.1002/jgre.20141.

Viviano-Beck, C. E., F. P. Seelos, S. L. Murchie, E. G. Kahn, K. D. Seelos, H. W. Taylor, K. Taylor, B. L. Ehlmann, S. M. Wisemann, J. F. Mustard, and M. F. Morgan (2014) Revised CRISM spectral parameters and summary products based on the currently detected mineral diversity on Mars. Journal of Geophysical Research, 119, 1403-1431 10.1002/2014JE004627.

Walter, L. S. and J. W. Salisbury (1989) Spectral characterization of igneous rocks in the 8- to 12-micron region. Journal of Geophysical Research, 94, 9203-9213 10.1029/JB094iB07p09203.

Weitz, C. M., M. D. Lane, M. Staid, and E. N. Dobrea (2008) Gray hematite distribution and formation in Ophir and Candor chasmata. Journal of Geophysical Research, 113, E0201610.1029/2007JE002930.

Weitz, C. M., E. Z. Noe Dobrea, M. D. Lane, and A. T. Knudson (2012) Geologic relationships between gray hematite, sulfates, and clays in Capri Chasma. Journal of Geophysical Research, 117, E00J0910.1029/2012JE004092.

Tables

Table 1: THEMIS Spectral Bands

Band	Center Wavelength (μm)	Width (μm) FWHM*
1	6.78	1.01
2	6.78	1.01
3	7.93	1.09
4	8.56	1.16
5	9.35	1.20
6	10.21	1.10
7	11.04	1.19
8	11.79	1.07
9	12.57	0.81
10	14.88	0.87

*Full width at half maximum transmission

Table 2: THEMIS high bulk SiO_2 composition locations

Region	THEMIS ID	Latitude (°N)	Longitude (°E)
a	I36988019	33.6	60.4
b	I01995006	34.1	64.9
c	I36688013	30.0	74.1
d	I01595009	24.5	79.9

Figure Captions

Figure 1. The Nilosyrtis Mensae region showing elevation (color) with THEMIS global infrared mosaic (shading). The white arrows show the locations of TIR detected high bulk SiO_2 surfaces and the white outlines show the approximate locations of hydrated compositions identified in Figure 4. The image is centered near 70°E, 29°N.

Figure 2. THEMIS bands 9–6–4 DCS images (left) and WAC data (right) covering the high bulk SiO_2 surfaces denoted in Figures 1 and 4. Images a–d are arranged from west to east and are listed in Table 2. The background grayscale image is the THEMIS global infrared mosaic. Yellow colors in the DCS images and low WAC values indicate the presence of high SiO_2 surfaces. Surfaces with a spectral contrast of <0.03 in emissivity (likely indicating dust mantled surfaces; e.g., *Ruff and Christensen*, 2002) are excluded from the WAC determination.

Figure 3. The four TIR spectral units throughout the region identified in THEMIS data (top). High bulk SiO_2 surfaces are only found in the four locations shown in Figures 1 and 2. Surface dust coincides with high albedo surfaces and basalt coincides with regional low albedo surfaces. The olivine-rich basalt is only present in the southeast portion of the study area in the Nili Fossae region. The four high SiO_2 locations (bottom) show consistent short wavelength absorptions. The signature is somewhat subdued and less prominent in TIR region c (THEMIS image I36688013) relative to the others, consistent with its orange rather than yellow color in the DCS image shown in Figure 2.

Figure 4. 1.9 μm hydration absorption index map constructed using individually stretched CRISM multispectral survey images (listed in the supplementary online material). The white arrows denote the locations of TIR detected high SiO_2 surfaces. Yellow arrows show the locations of the three example high resolution CRISM images shown in Figures 7–9. The hydrated surfaces are much more extensive than the high bulk SiO_2 surfaces, but both compositions occur in similar terrains at the base of a topographic scarp. The image is centered near 70°E, 29°N.

Figure 5. CRISM MSP spectra covering the two westernmost high bulk SiO_2 locations identified using THEMIS data (TIR region a). The red spectrum (0000867D_01; 34.30°N, 64.97°E) shows what may be a faint hydration absorption feature near 1.93 μm where the THEMIS data show strong indications of a surface dominated by high Si phases (shown in Figure 2b). The green (000034DB_05; 33.47°N, 60.42°E) and blue (00004A7D_07; 33.50°N, 60.42°E) spectra show distinct 1.4, 2.2–2.3, and 2.29 μm absorption features consistent with the presence of Fe/Mg-smectite and hydrated silica phases. These compositions are coincident with the westernmost high SiO_2 surfaces shown in Figure 2a.

Figure 6. CRISM full resolution spectra from images FRT0000527D_07 (phyllosilicate and hydrated; near 29.3°N, 73.3°E; NIR example 1) and FRT0000D452_07 (hydrated silica and Mg-carbonate; near 27.8°N, 76.6°E; NIR example 2). These are the four types of alteration spectra identified throughout the Nilosyrtis Mensae region. The hydrated spectrum (cyan) contains only a 1.9 μm absorption and other diagnostic absorptions may be too weak to identify or were present in both the numerator and denominator of the spectral ratio.

Figure 7. CRISM image FRT0000527D_07 (NIR example 1) centered near 29.3°N, 73.3°E. Colors show the strength of the 1.9 and 2.29 μm absorption indices (BD1900 from 0.083 to 0.138 and BD2290 from –0.005 to 0.011) with CTX image P06_003231_2090_XI_29N286W used for shading. The arrows denote two locations with strong 1.9 μm absorptions, but variable 2.29 μm absorptions (strong in the southeast and weak in the northwest).

Figure 8. CRISM image FRT0000D452_07 (NIR example 2) centered near 27.8°N, 76.4°E. Colors show the strength of the 1.9, 2.29, 2.25, and 2.5 μm absorption indices (BD1900 from 0.077 to 0.136, BD2290 from –0.012 to 0.014, BD2250 from –0.011 to 0.013, and BD2500 from –0.027 to 0.000) with CTX image B03_010707_2080_XN_28N283W used for shading. The arrows denote specific locations indicative of Fe/Mg-smectites, hydrated silica, and Mg-carbonates.

Figure 9. CRISM image FRT0000C79D_07 (NIR example 3) centered near 24.8°N, 80.4°E. Colors show the strength of the 1.9 and 2.29 μm absorption indices (BD1900 from 0.080 to 0.130 and BD2290 from –0.011 to 0.011) with CTX image P15_006791_2050_XN_25N279W used for shading. The arrows denote two locations with strong 1.9 μm absorptions, but variable 2.29 μm absorptions (strong in the south and weak in the north).

Figure 10. CTX images showing the high SiO_2 surfaces identified using THEMIS spectral data. Images a–d cover the same locations as THEMIS images a–d shown in Figure 2 and listed in Table 2. White circles and ovals denote high SiO_2 surfaces, which typically coincide with moderate toned surfaces with smooth textures at the 5.5 m scale of the image sampling. CTX images are (a) G05_020083_2134_XI_33N299W, (b) B16_015916_2167_XN_36N295W, (c) G03_019555_2119_XI_31N286W, and (d) D14_032583_2056_XI_25N280W.

Figure 11. HiRISE images showing surface textures of phyllosilicate (top images and bottom left image) and carbonate (bottom right image) bearing terrains. The phyllosilicates and carbonates are typically found within highly fractured and somewhat light-toned materials. The phyllosilicates can also be found within sequences of layered materials, such as the thick light-toned layer running across the center of the image shown in the top right. HiRISE images PSP_006791_2050 (top left and right;

NIR example 3), PSP_003231_2095 (bottom left; NIR example 1), PSP_10707_2080 (bottom right; NIR example 2).

Figure 12. HiRISE images showing hydrated silica surfaces (top) and surfaces of unknown composition containing only a 1.9 μm absorption (bottom). Both compositional types show relatively smooth surface textures in contrast to the immediately adjacent heavily fractured terrains that commonly contain spectral absorptions consistent with Fe/Mg-smectites. HiRISE images PSP_006791_2050 (top; NIR example 3) and PSP_003231_2095 (bottom; NIR example 1).

Figure 13. Comparison of THEMIS spectra of martian high bulk SiO_2 terrains. The Nilosyrtis Mensae high SiO_2 surfaces are similar to high SiO_2 surfaces in western Hellas Basin that are dominated by up to 80% high Si phases. The short wavelength absorption between ~8–12 μm is more distinct than other high SiO_2 terrains, such as those found near Antoniadi Crater and TES global surface type 2. This indicates that higher abundances of high Si phases are likely present at the Nilosyrtis Mensae and western Hellas Basin high SiO_2 surfaces.

Supplementary Material

Table S1: CRISM multispectral images used in Figure 4

36–42°N

MSP00003070_03_IF214L_TRR3
MSP00003070_05_IF214L_TRR3
MSP000031A7_03_IF214L_TRR3
MSP000033DA_03_IF214L_TRR3
MSP000033DA_05_IF214L_TRR3
MSP000034CB_05_IF214L_TRR3
MSP000035DF_05_IF214L_TRR3
MSP000035DF_07_IF214L_TRR3
MSP0000402A_05_IF214L_TRR3
MSP000042D5_05_IF214L_TRR3
MSP000043E0_05_IF214L_TRR3
MSP000046C8_03_IF214L_TRR3
MSP00004A7D_07_IF214L_TRR3
MSP00004EB4_01_IF213L_TRR3
MSP00006FDE_03_IF214L_TRR3
MSP000072F6_05_IF214L_TRR3
MSP00007779_01_IF214L_TRR3
MSP00008CF8_01_IF214L_TRR3
MSP00010409_01_IF214L_TRR3
MSP000105E2_01_IF214L_TRR3
MSP000108A7_01_IF214L_TRR3
MSP00011045_01_IF214L_TRR3
MSP00012E63_01_IF213L_TRR3
MSP00013C15_01_IF214L_TRR3
MSP000149B8_01_IF214L_TRR3
MSP000159AC_03_IF214L_TRR3
MSP0001AADA_01_IF214L_TRR3
MSP0002602A_01_IF214L_TRR3
MSP0002602A_03_IF214L_TRR3

33–36°N

MSP000031EC_01_IF214L_TRR3
MSP000038D8_07_IF214L_TRR3
MSP00003A7C_01_IF214L_TRR3
MSP00003C3F_05_IF214L_TRR3
MSP00004732_01_IF214L_TRR3
MSP00004F12_01_IF214L_TRR3
MSP00004F12_03_IF214L_TRR3
MSP000053E3_03_IF214L_TRR3
MSP000055B2_01_IF214L_TRR3
MSP00005D87_01_IF213L_TRR3
MSP00008026_01_IF214L_TRR3
MSP0000867D_01_IF214L_TRR3
MSP0000C8BC_01_IF214L_TRR3
MSP00010CE9_01_IF213L_TRR3
MSP00014A3B_05_IF214L_TRR3
MSP00014CC8_01_IF214L_TRR3
MSP0001511D_01_IF214L_TRR3
MSP00021C02_03_IF214L_TRR3
MSP00026079_03_IF214L_TRR3

26–32°N

MSP00002F1D_03_IF214L_TRR3
MSP00002F1D_05_IF214L_TRR3
MSP00002FE4_03_IF214L_TRR3
MSP00002FE4_05_IF214L_TRR3
MSP00003342_03_IF214L_TRR3
MSP00003342_05_IF214L_TRR3
MSP0000343F_03_IF214L_TRR3
MSP0000343F_05_IF214L_TRR3
MSP0000366C_01_IF214L_TRR3
MSP000036A9_03_IF214L_TRR3
MSP000036A9_05_IF214L_TRR3
MSP000037E8_03_IF214L_TRR3
MSP000037E8_05_IF214L_TRR3
MSP0000397F_05_IF214L_TRR3
MSP0000397F_07_IF214L_TRR3
MSP00003C77_07_IF214L_TRR3
MSP00003F2C_03_IF214L_TRR3
MSP00003F2C_05_IF214L_TRR3
MSP0000412D_05_IF214L_TRR3
MSP00004267_01_IF214L_TRR3
MSP000049C0_07_IF214L_TRR3
MSP00004FD2_01_IF214L_TRR3
MSP0000516B_01_IF214L_TRR3
MSP000052D4_01_IF214L_TRR3
MSP000052D4_03_IF214L_TRR3
MSP00005AC1_01_IF214L_TRR3
MSP00005B10_01_IF213L_TRR3
MSP00006118_03_IF214L_TRR3
MSP00006119_01_IF213L_TRR3
MSP0000627F_01_IF213L_TRR3
MSP00007527_01_IF214L_TRR3
MSP000076C1_01_IF214L_TRR3
MSP00007A27_07_IF214L_TRR3
MSP00007C18_01_IF214L_TRR3
MSP000080AF_03_IF214L_TRR3
MSP000080AF_05_IF214L_TRR3
MSP00008E3E_01_IF214L_TRR3
MSP00008E3E_03_IF214L_TRR3
MSP0000902D_01_IF214L_TRR3
MSP0000941C_01_IF214L_TRR3
MSP0000B5AC_01_IF214L_TRR3
MSP0000C752_01_IF214L_TRR3
MSP0000CE73_01_IF214L_TRR3
MSP0000D48B_01_IF213L_TRR3
MSP000106BC_03_IF214L_TRR3
MSP000106BD_01_IF213L_TRR3
MSP00010AB0_01_IF214L_TRR3
MSP00010D27_05_IF214L_TRR3
MSP00010F57_01_IF214L_TRR3
MSP0001138D_01_IF214L_TRR3
MSP0001185D_03_IF214L_TRR3
MSP00011D14_01_IF213L_TRR3
MSP00012F58_01_IF214L_TRR3
MSP00013755_01_IF214L_TRR3
MSP00013795_01_IF213L_TRR3
MSP0001396C_01_IF214L_TRR3
MSP00014007_01_IF214L_TRR3
MSP0001423B_05_IF214L_TRR3
MSP0001423B_07_IF214L_TRR3

MSP000148C2_01_IF214L_TRR3
MSP00015218_01_IF214L_TRR3
MSP0001553E_01_IF213L_TRR3
MSP0001582D_05_IF214L_TRR3
MSP0001A9F9_01_IF214L_TRR3
MSP0001ACED_01_IF214L_TRR3
MSP0001BA1F_01_IF214L_TRR3
MSP0001C6C6_01_IF213L_TRR3
MSP0001CA9A_01_IF213L_TRR3
MSP000233B6_01_IF214L_TRR3
MSP00023778_01_IF214L_TRR3
MSP0002440D_01_IF214L_TRR3
MSP000248F6_01_IF214L_TRR3
MSP00026155_01_IF214L_TRR3

23–26°N
MSP0000366C_01_IF214L_TRR3
MSP000037E8_03_IF214L_TRR3
MSP0000397F_05_IF214L_TRR3
MSP00003F2C_03_IF214L_TRR3
MSP00004FD2_01_IF214L_TRR3
MSP000052D4_01_IF214L_TRR3
MSP00005AC1_01_IF214L_TRR3
MSP000062D3_01_IF214L_TRR3
MSP000062D3_03_IF214L_TRR3
MSP00007A27_05_IF214L_TRR3
MSP00007A27_07_IF214L_TRR3
MSP00007C18_01_IF214L_TRR3
MSP000080AF_03_IF214L_TRR3
MSP0000902D_01_IF214L_TRR3
MSP0000941C_01_IF214L_TRR3
MSP0000B32F_01_IF214L_TRR3
MSP0000B5AC_01_IF214L_TRR3
MSP000106BC_03_IF214L_TRR3
MSP00010AB0_01_IF214L_TRR3
MSP0001185D_03_IF214L_TRR3
MSP00012F58_01_IF214L_TRR3
MSP00013755_01_IF214L_TRR3
MSP0001396C_01_IF214L_TRR3
MSP00014007_01_IF214L_TRR3
MSP0001423B_05_IF214L_TRR3
MSP00015218_01_IF214L_TRR3
MSP0001582D_05_IF214L_TRR3
MSP0001969A_01_IF213L_TRR3
MSP0001ACED_01_IF214L_TRR3
MSP0001C6C6_01_IF213L_TRR3
MSP00026F8F_01_IF213L_TRR3

29–30°N
MSP00003ACB_07_IF214L_TRR3
MSP000040BA_03_IF214L_TRR3
MSP0000443E_05_IF214L_TRR3
MSP0000487C_07_IF214L_TRR3
MSP0000560D_01_IF214L_TRR3
MSP00005C0B_03_IF214L_TRR3
MSP00006D43_07_IF214L_TRR3

Table S2: CRISM sample and line numbers used for spectra shown in Figure 5

Image ID	Numerator (column; row)	Denominator (column; row)
MSP00004A7D_07	28–33; 152–155	28–33; 166–170
MSP000034CB_05	43–47; 296–298	43–47; 325–332
MSP0000867D_01	50–51; 288–291	50–51; 326–335

Table S3: CRISM sample and line numbers used for spectra shown in Figure 6

Image ID	Label	Numerator (column; row)	Denominator (column; row)
FRT0000D452_07	Hydrated Silica	34–43; 277–287	34–43; 160–170
FRT0000527D_07	Phyllosilicate	383–385; 418–420	383–385; 468–471
FRT0000D452_07	Mg-Carbonate	193–197; 204–207	193–197; 65–70
FRT0000527D_07	Hydrated	163–167; 161–165	163–167; 110–120

1045 **Table S4:** THEMIS latitude and longitude ranges used for high SiO_2 spectra shown in Figure 3

Region	THEMIS ID	Latitude (°N)	Longitude (°E)
a	I36988019	33.4704–33.5025	60.3993–60.4145
b	I01995006	34.1807–34.2482	64.9746–65.0185
c	I36688013	30.6480–30.6598	74.1708–74.1775
d	I01595009	24.3890–24.3941	79.6672–79.6790

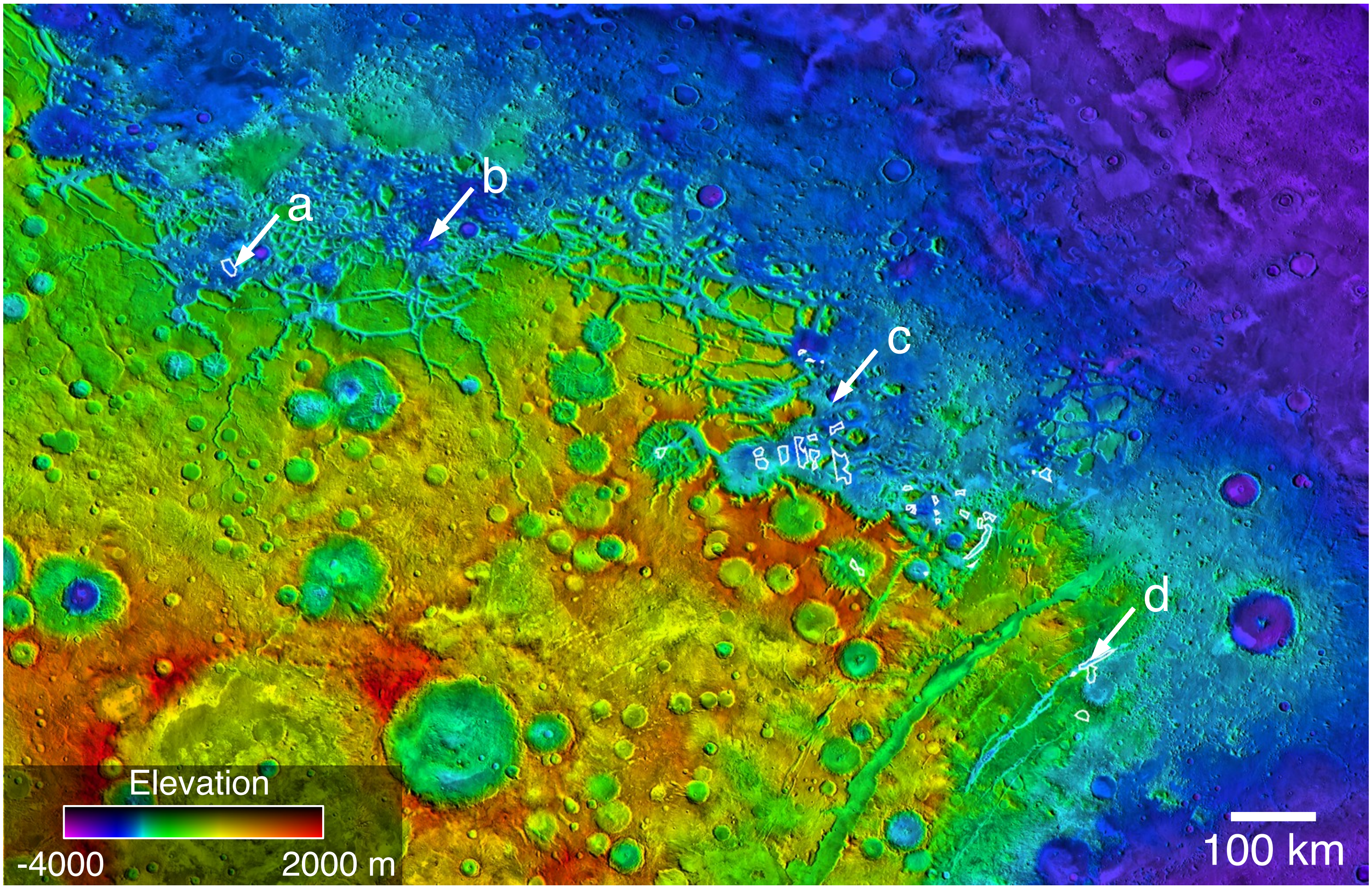

Figure 1. The Nilosyrtis Mensae region showing elevation (color) with THEMIS global infrared mosaic (shading). The white arrows show the locations of TIR detected high bulk SiO_2 surfaces and the white outlines show the approximate locations of hydrated compositions identified in Figure 4. The image is centered near 70°E, 29°N.

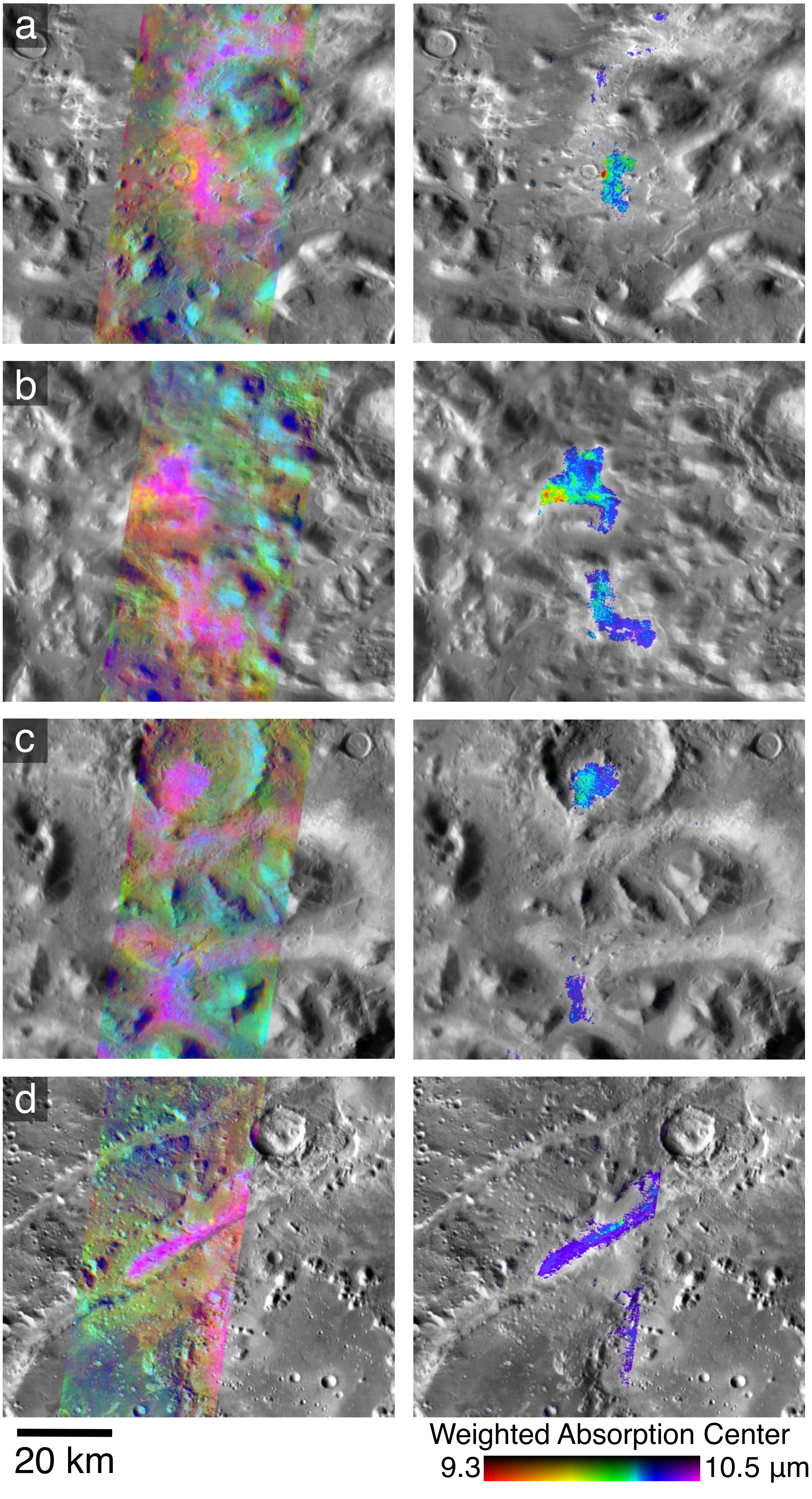

Figure 2. THEMIS bands 9–6–4 DCS images (left) and WAC data (right) covering the high bulk SiO_2 surfaces denoted in Figures 1 and 4. Images a–d are arranged from west to east and are listed in Table 2. The background grayscale image is the THEMIS global infrared mosaic. Yellow colors in the DCS images and low WAC values indicate the presence of high SiO_2 surfaces. Surfaces with a spectral contrast of <0.03 in emissivity (likely indicating dust mantled surfaces; e.g., *Ruff and Christensen*, 2002) are excluded from the WAC determination.

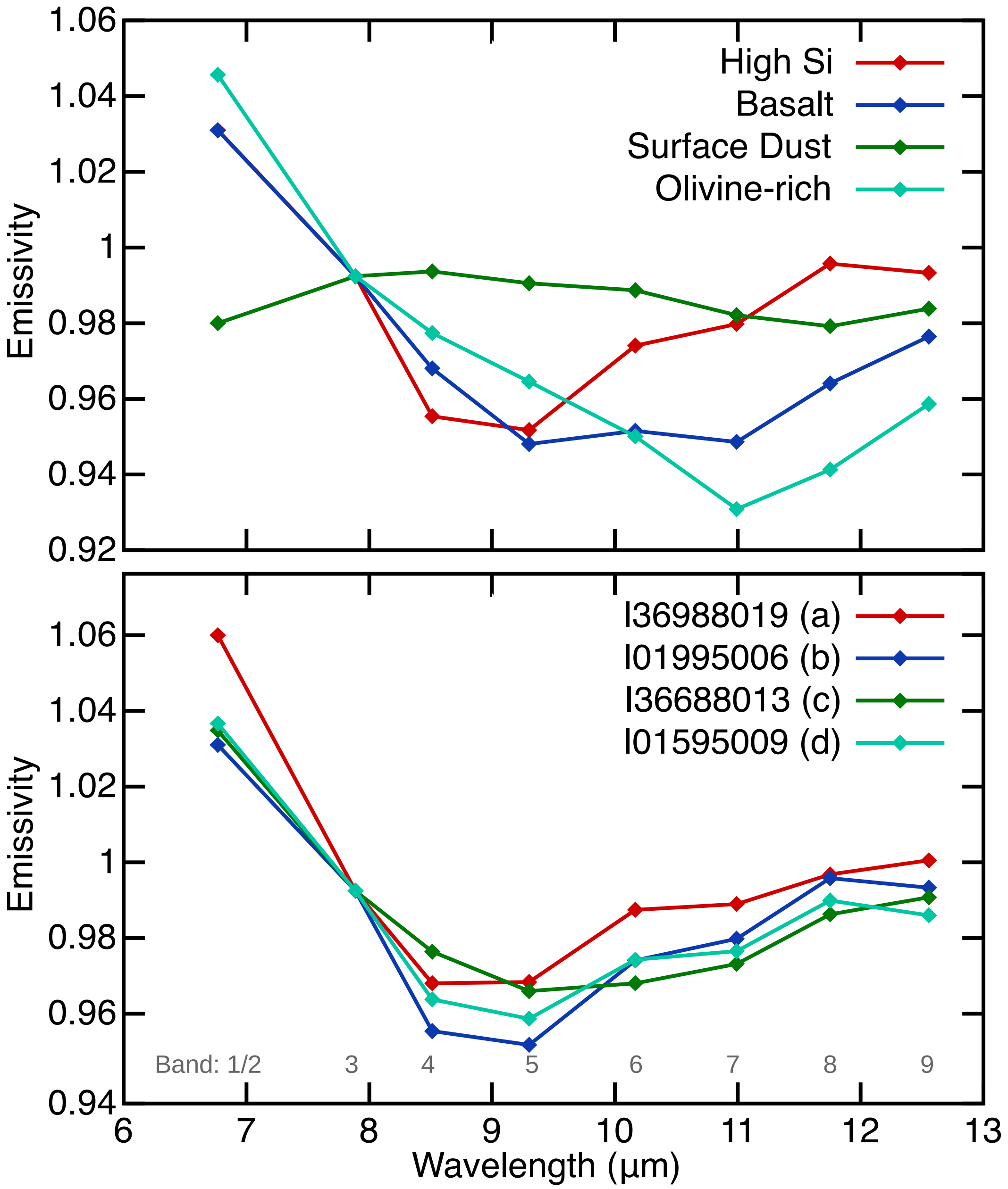

Figure 3. The four TIR spectral units throughout the region identified in THEMIS data (top). High bulk SiO_2 surfaces are only found in the four locations shown in Figures 1 and 2. Surface dust coincides with high albedo surfaces and basalt coincides with regional low albedo surfaces. The olivine-rich basalt is only present in the southeast portion of the study area in the Nili Fossae region. The four high SiO_2 locations (bottom) show consistent short wavelength absorptions. The signature is somewhat subdued and less prominent in TIR region c (THEMIS image I36688013) relative to the others, consistent with its orange rather than yellow color in the DCS image shown in Figure 2.

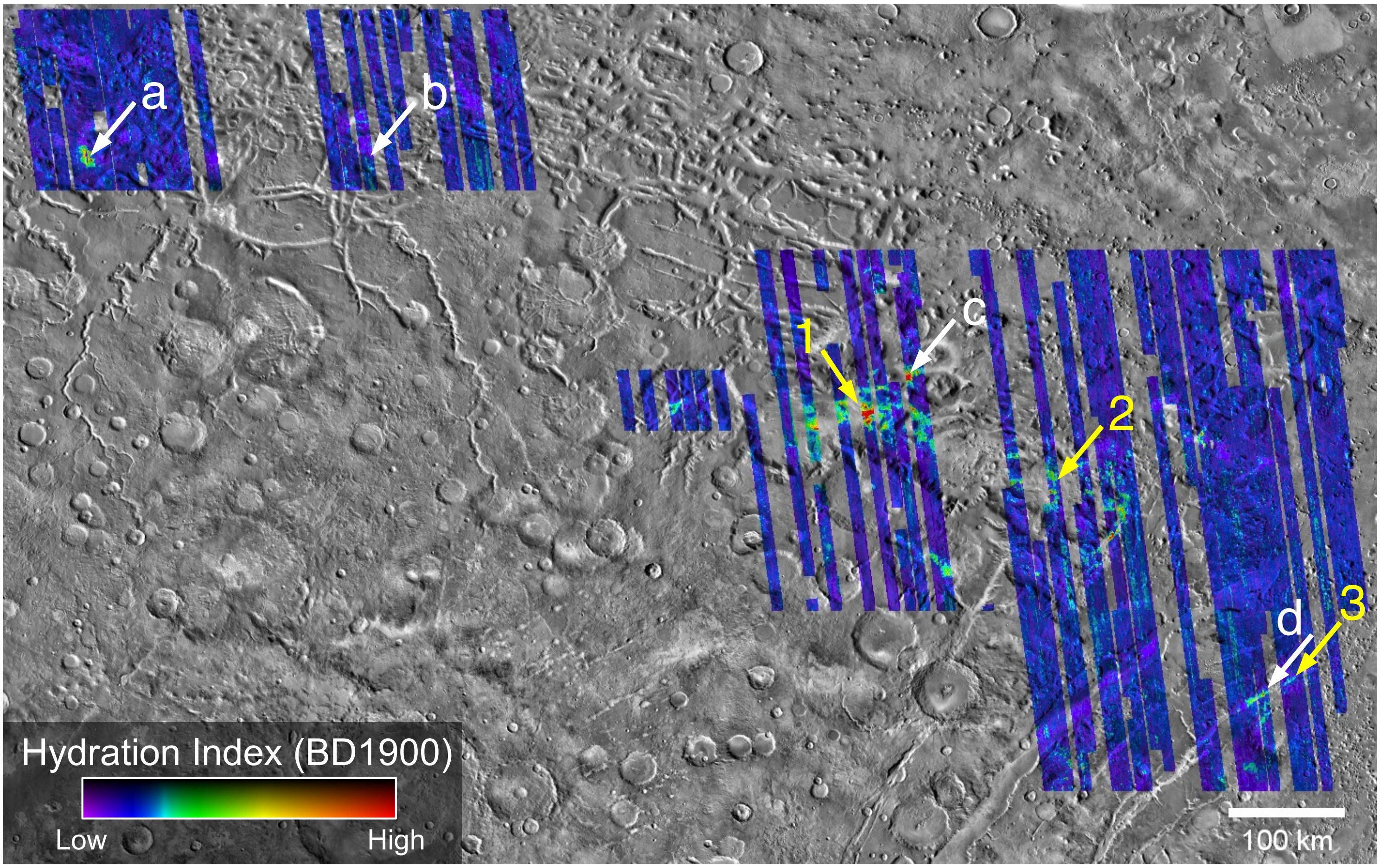

Figure 4. 1.9 µm hydration absorption index map constructed using individually stretched CRISM multispectral survey images (listed in the supplementary online material). The white arrows denote the locations of TIR detected high SiO_2 surfaces. Yellow arrows show the locations of the three example high resolution CRISM images shown in Figures 7–9. The hydrated surfaces are much more extensive than the high bulk SiO_2 surfaces, but both compositions occur in similar terrains at the base of a topographic scarp. The image is centered near 70°E, 29°N.

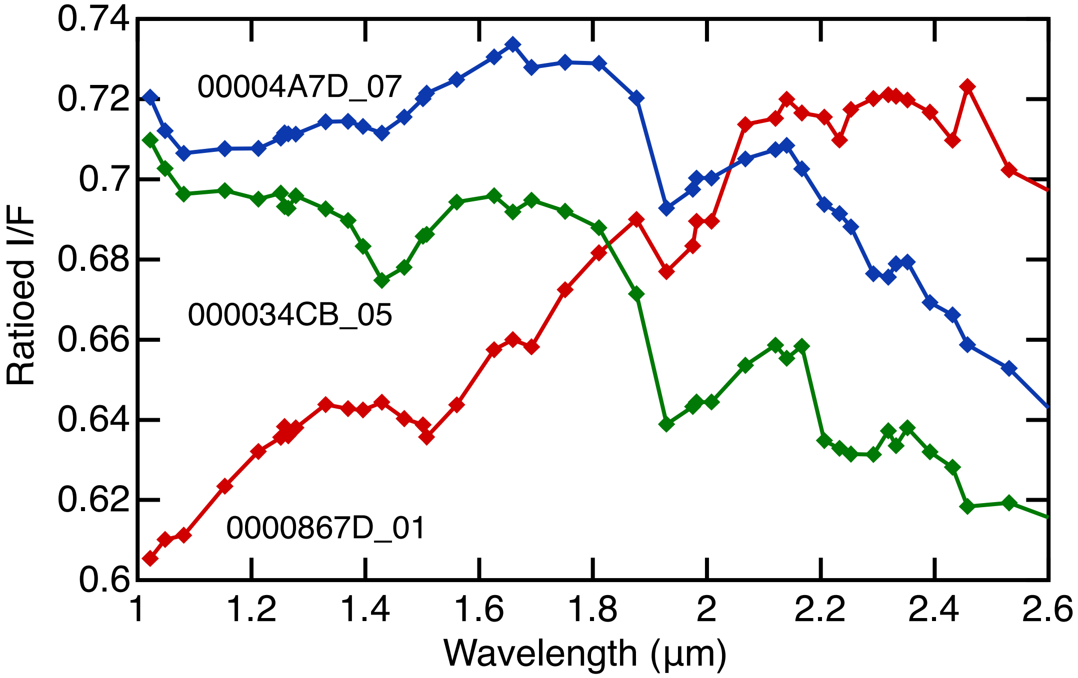

Figure 5. CRISM MSP spectra covering the two westernmost high bulk SiO_2 locations identified using THEMIS data (TIR region a). The red spectrum (0000867D_01; 34.30°N, 64.97°E) shows what may be a faint hydration absorption feature near 1.93 µm where the THEMIS data show strong indications of a surface dominated by high Si phases (shown in Figure 2b). The green (000034DB_05; 33.47°N, 60.42°E) and blue (00004A7D_07; 33.50°N, 60.42°E) spectra show distinct 1.4, 2.2–2.3, and 2.29 µm absorption features consistent with the presence of Fe/Mg-smectite and hydrated silica phases. These compositions are coincident with the westernmost high SiO_2 surfaces shown in Figure 2a.

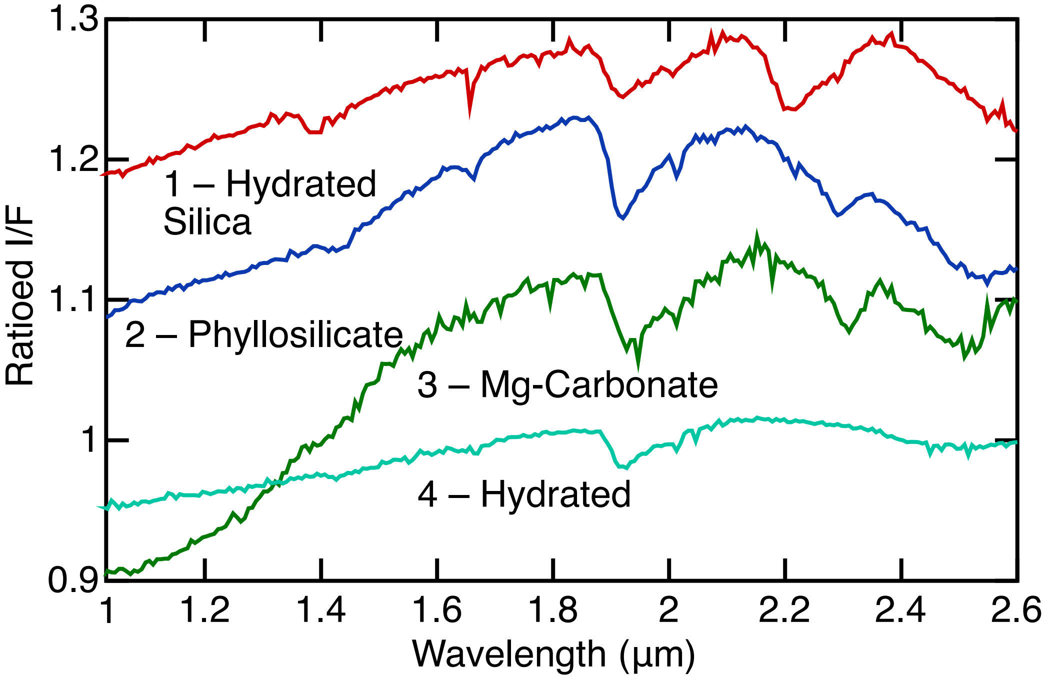

Figure 6. CRISM full resolution spectra from images FRT0000527D_07 (phyllosilicate and hydrated; near 29.3°N, 73.3°E; NIR example 1) and FRT0000D452_07 (hydrated silica and Mg-carbonate; near 27.8°N, 76.6°E; NIR example 2). These are the four types of alteration spectra identified throughout the Nilosyrtis Mensae region. The hydrated spectrum (cyan) contains only a 1.9 µm absorption and other diagnostic absorptions may be too weak to identify or were present in both the numerator and denominator of the spectral ratio.

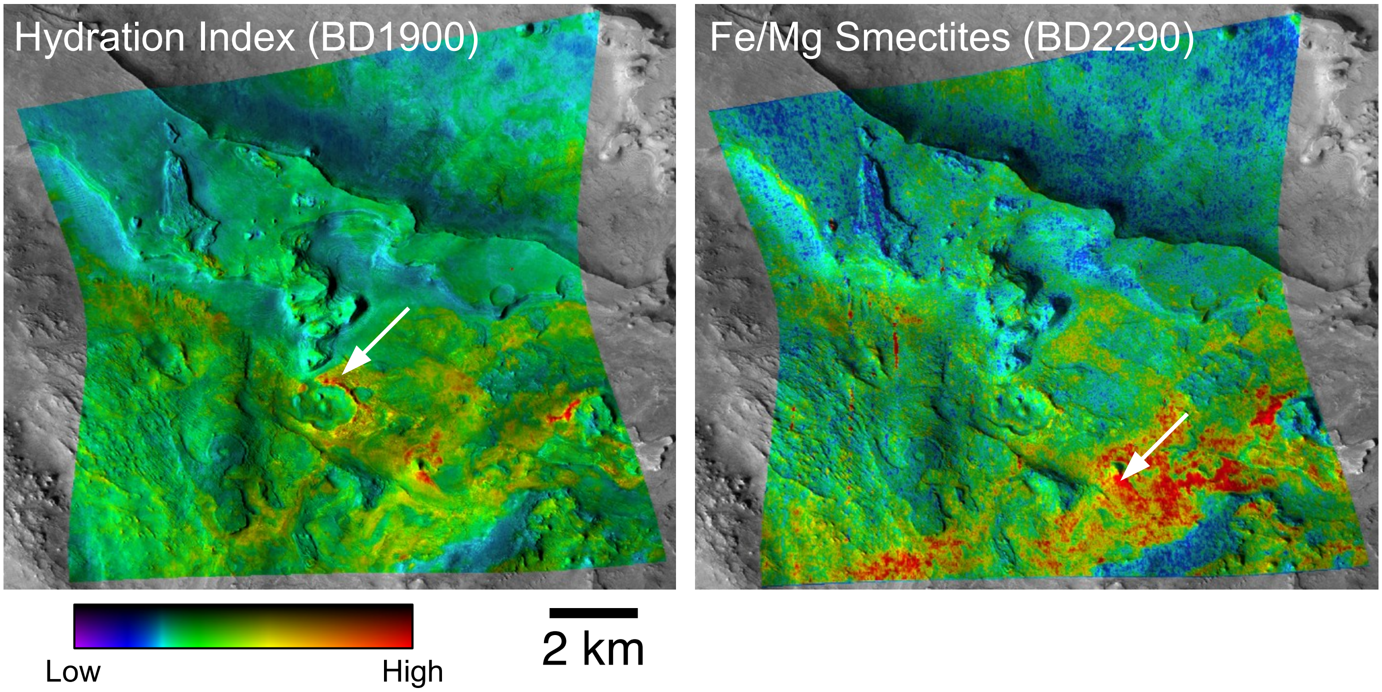

Figure 7. CRISM image FRT0000527D_07 (NIR example 1) centered near 29.3°N, 73.3°E. Colors show the strength of the 1.9 and 2.29 μm absorption indices (BD1900 from 0.083 to 0.138 and BD2290 from –0.005 to 0.011) with CTX image P06_003231_2090_XI_29N286W used for shading. The arrows denote two locations with strong 1.9 μm absorptions, but variable 2.29 μm absorptions (strong in the southeast and weak in the northwest).

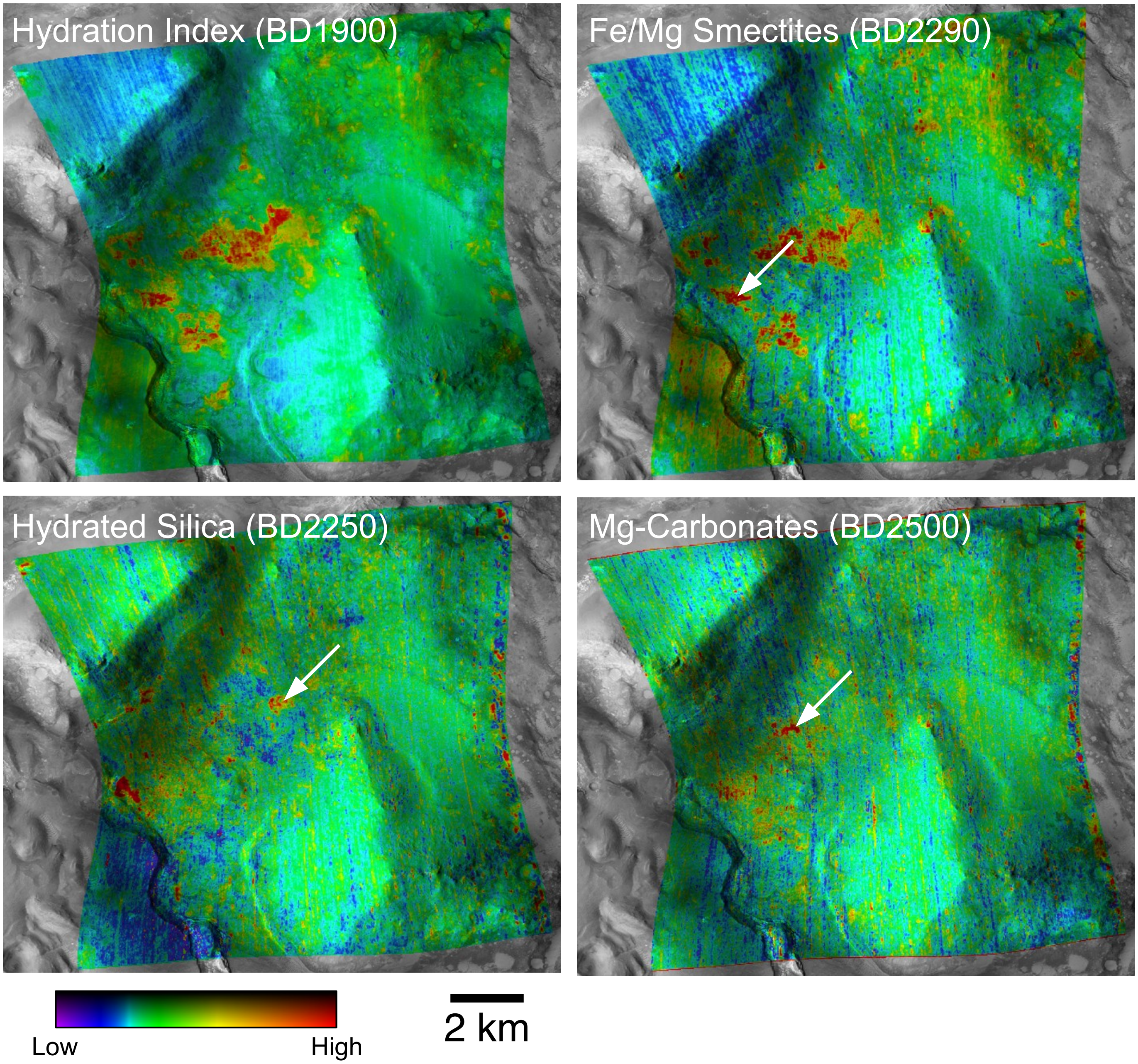

Figure 8. CRISM image FRT0000D452_07 (NIR example 2) centered near 27.8°N, 76.4°E. Colors show the strength of the 1.9, 2.29, 2.25, and 2.5 μm absorption indices (BD1900 from 0.077 to 0.136, BD2290 from –0.012 to 0.014, BD2250 from –0.011 to 0.013, and BD2500 from –0.027 to 0.000) with CTX image B03_010707_2080_XN_28N283W used for shading. The arrows denote specific locations indicative of Fe/Mg-smectites, hydrated silica, and Mg-carbonates.

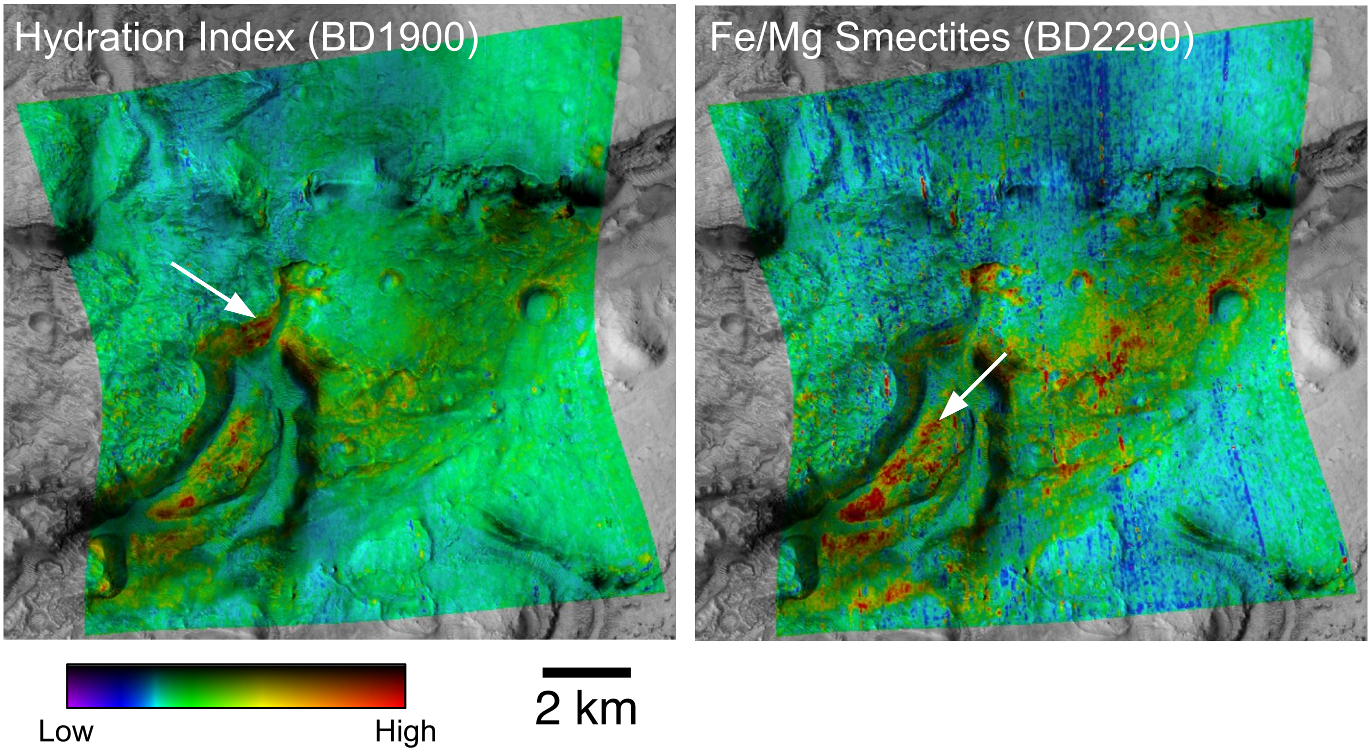

Figure 9. CRISM image FRT0000C79D_07 (NIR example 3) centered near 24.8°N, 80.4°E. Colors show the strength of the 1.9 and 2.29 μm absorption indices (BD1900 from 0.080 to 0.130 and BD2290 from –0.011 to 0.011) with CTX image P15_006791_2050_XN_25N279W used for shading. The arrows denote two locations with strong 1.9 μm absorptions, but variable 2.29 μm absorptions (strong in the south and weak in the north).

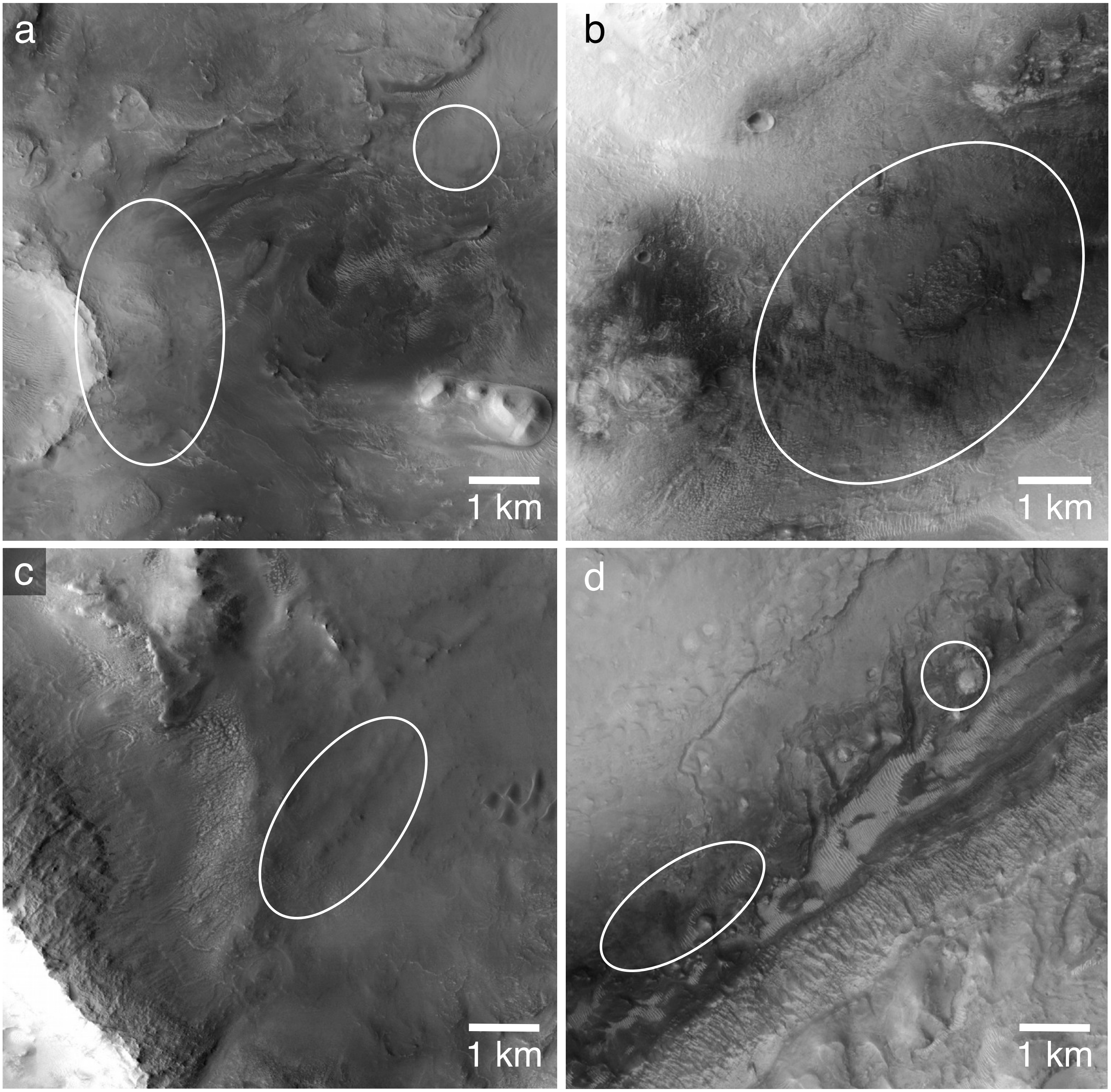

Figure 10. CTX images showing the high SiO_2 surfaces identified using THEMIS spectral data. Images a–d cover the same locations as THEMIS images a–d shown in Figure 2 and listed in Table 2. White circles and ovals denote high SiO_2 surfaces, which typically coincide with moderate toned surfaces with smooth textures at the 5.5 m scale of the image sampling. CTX images are (a) G05_020083_2134_XI_33N299W, (b) B16_015916_2167_XN_36N295W, (c) G03_019555_2119_XI_31N286W, and (d) D14_032583_2056_XI_25N280W.

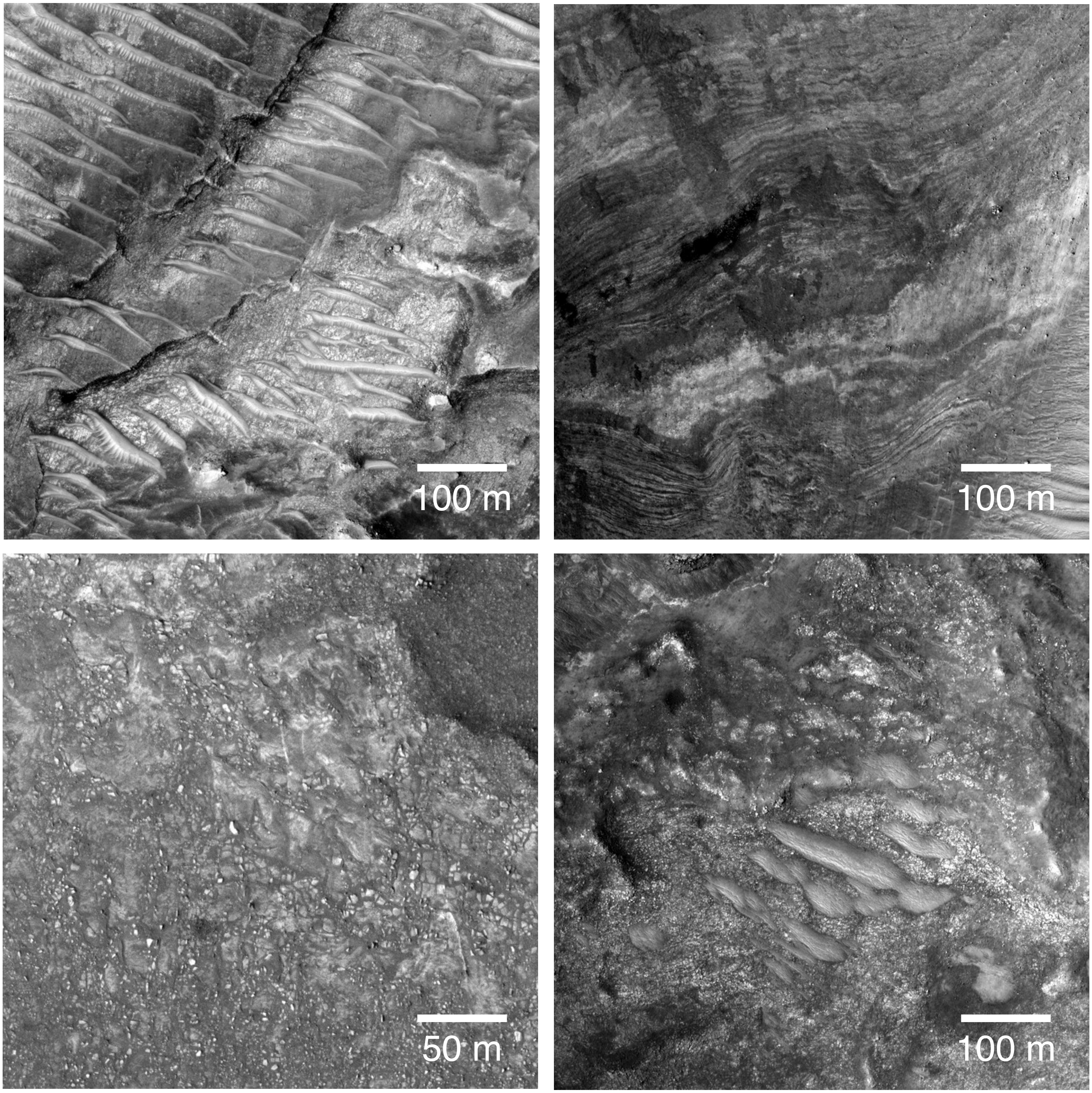

Figure 11. HiRISE images showing surface textures of phyllosilicate (top images and bottom left image) and carbonate (bottom right image) bearing terrains. The phyllosilicates and carbonates are typically found within highly fractured and somewhat light-toned materials. The phyllosilicates can also be found within sequences of layered materials, such as the thick light-toned layer running across the center of the image shown in the top right. HiRISE images PSP_006791_2050 (top left and right; NIR example 3), PSP_003231_2095 (bottom left; NIR example 1), PSP_10707_2080 (bottom right; NIR example 2).

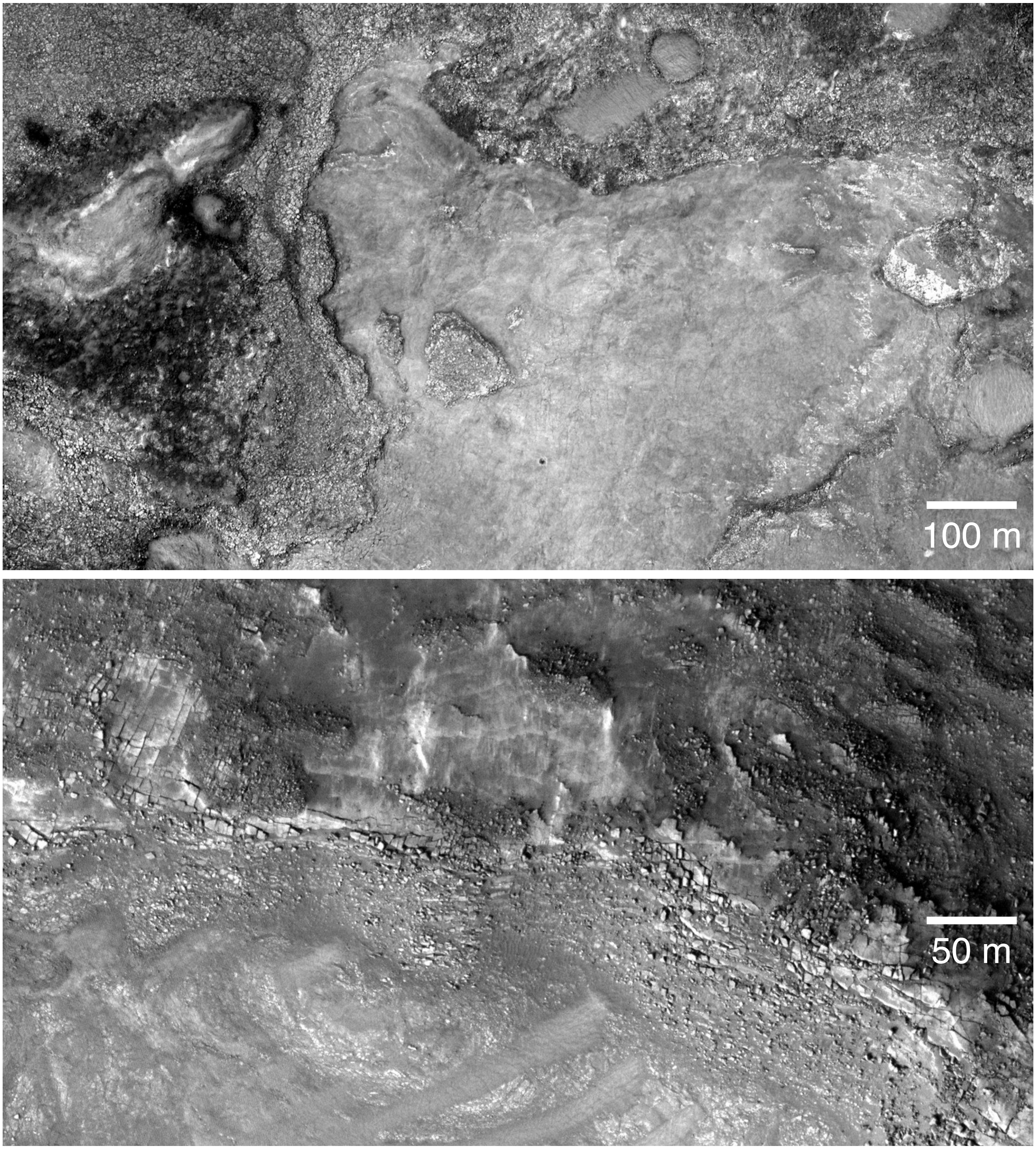

Figure 12. HiRISE images showing hydrated silica surfaces (top) and surfaces of unknown composition containing only a 1.9 µm absorption (bottom). Both compositional types show relatively smooth surface textures in contrast to the immediately adjacent heavily fractured terrains that commonly contain spectral absorptions consistent with Fe/Mg-smectites. HiRISE images PSP_006791_2050 (top; NIR example 3) and PSP_003231_2095 (bottom; NIR example 1).

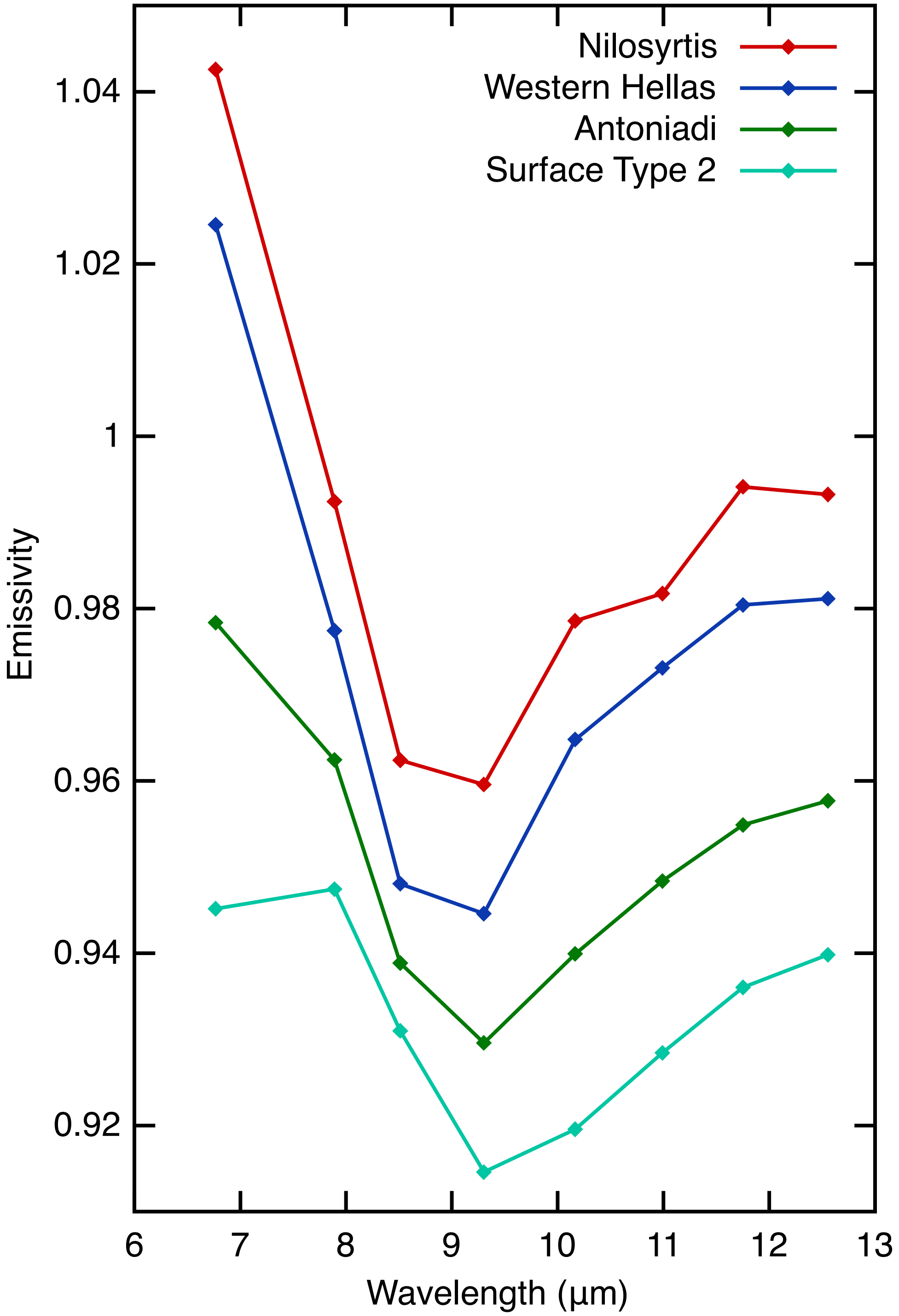

Figure 13. Comparison of THEMIS spectra of martian high bulk SiO_2 terrains. The Nilosyrtis Mensae high SiO_2 surfaces are similar to high SiO_2 surfaces in western Hellas Basin that are dominated by up to 80% high Si phases. The short wavelength absorption between ~8–12 μm is more distinct than other high SiO_2 terrains, such as those found near Antoniadi Crater and TES global surface type 2. This indicates that higher abundances of high Si phases are likely present at the Nilosyrtis Mensae and western Hellas Basin high SiO_2 surfaces.